



**CHARACTERIZATION AND CONTROL OF CARBON DIOXIDE SEED  
PARTICLES IN PARTICLE IMAGE VELOCIMETRY**

Bartt G. Greene, Major, USMC

AFIT/GAE/ENY/08-M12

**DEPARTMENT OF THE AIR FORCE  
AIR UNIVERSITY**

***AIR FORCE INSTITUTE OF TECHNOLOGY***

---

---

**Wright-Patterson Air Force Base, Ohio**

APPROVED FOR PUBLIC RELEASE; DISTRIBUTION UNLIMITED

The views expressed in this thesis are those of the author and do not reflect the official policy or position of the United States Marine Corps, Department of Defense, or the United States Government.

AFIT/GAE/ENY/08-M12

**CHARACTERIZATION AND CONTROL OF CARBON DIOXIDE SEED  
PARTICLES IN PARTICLE IMAGE VELOCIMETRY**

THESIS

Presented to the Faculty

Department of Aeronautics and Astronautics

Graduate School of Engineering and Management

Air Force Institute of Technology

Air University

Air Education and Training Command

In Partial Fulfillment of the Requirements for the  
Degree of Master of Science in Aeronautical Engineering

Bartt G. Greene, BS

Major, USMC

March 2008

APPROVED FOR PUBLIC RELEASE; DISTRIBUTION UNLIMITED

AFIT/GAE/ENY/08-M12

**CHARACTERIZATION AND CONTROL OF CARBON DIOXIDE SEED  
PARTICLES IN PARTICLE IMAGE VELOCIMETRY**

Bartt G. Greene, BS

Major, USMC

Approved:

//Signed \_\_\_\_\_ 12 March 08 \_\_\_\_\_

Dr. Mark F. Reeder (Chairman)

Date

//Signed \_\_\_\_\_ 07 March 08 \_\_\_\_\_

Maj Richard Branam (Member)

Date

//Signed \_\_\_\_\_ 07 March 08 \_\_\_\_\_

Dr. Robert B. Greendyke (Member)

Date



### **Abstract**

Particle Image Velocimetry (PIV) data was acquired in two separate supersonic wind tunnels with carbon dioxide (CO<sub>2</sub>) particles utilized as the seed material. Previous work in clean seeding showed CO<sub>2</sub> could be used as seed material to produce velocity maps. This research provides the first quantitative assessment of particle response, particle size control via purge gas, and scalability using CO<sub>2</sub> particles. A variety of feed tube and shroud configurations, in combination with varying volumetric flow rates of purge air were measured using a laser diffraction device. The CO<sub>2</sub> particles were injected into the stilling chamber of two open-circuit blow down supersonic wind tunnels to obtain PIV measurements. Results from each tunnel produced accurate free stream velocity measurements and demonstrate the ability to perform a basic boundary layer analysis. A ten degree ramp placed in the test section of the smaller wind tunnel produced a shock wave which allowed for the characterization of the time response of the CO<sub>2</sub> particles as they crossed the shock wave. This time response was compared with theoretical time responses of varying diameter CO<sub>2</sub> particles in order to characterize the spherical diameter of the actual CO<sub>2</sub> particles in the test section. Purge air fed into the shroud tube was used to demonstrate the ability to alter the size of particles. A scale up was performed to demonstrate the applicability of the clean seeding technique to different size wind tunnels. Initial particle measurements demonstrate the ability to control the size of CO<sub>2</sub> particles.

For my daughter

## **Acknowledgments**

Dr. Mark Reeder provided much needed insight and direction for this thesis. I also thank him for his patience, as I'm sure he thought I would never get started much less finished.

I'd also like to thank my mother for her editorial contributions despite her always busy schedule.

John Hixenbaugh contributed immensely to this experiment and paper. He was my "go to" man for equipment, questions or a helping hand in the lab. His knowledge of lab procedures and equipment was invaluable. I'd also like to thank Jay, Chris, Shawn, Wilbur and Barry for their contributions.

Bartt G. Greene

MAJ      USMC

## Table of Contents

	Page
<b>Abstract.....</b>	<b>v</b>
<b>Acknowledgments.....</b>	<b>vii</b>
<b>Table of Contents .....</b>	<b>viii</b>
<b>List of Figures .....</b>	<b>x</b>
<b>List of Tables.....</b>	<b>xiii</b>
<b>1. Introduction .....</b>	<b>1</b>
1. 1 Motivation and Hypothesis .....	1
1. 2 Research Focus and Goals.....	7
<b>2. Overview and Literature Review.....</b>	<b>8</b>
2. 1 PIV Overview.....	8
2. 2 Particle Sizing Using Laser Diffraction .....	12
2. 3 Particle Characterization Using PIV and Relaxation Time.....	16
2. 4 Recent Research and Literature.....	23
<b>3. Methodology .....</b>	<b>25</b>
3. 1 Experimental Apparatus and Setup .....	25
3. 1. 1 Malvern Spraytec System Set-up and Procedure .....	25
3. 1. 2 Wind tunnel set-up.....	26
3. 1. 3 PIV set up .....	29
3. 2 Experimental Procedure .....	35
3. 2. 1 Malvern testing.....	35
3. 2. 2 PIV runs.....	39
<b>4. Results and Analysis.....</b>	<b>46</b>
4. 1 Malvern Particle Size Characterization.....	46
4. 2 Labview Analysis.....	55
4. 3 PIV Analysis .....	57
4. 4 Sources of Error .....	78
<b>5. Conclusions and Recommendations .....</b>	<b>80</b>

5. 1	Results Summary and Conclusion.....	80
5. 2	Desired Impact of this Research.....	83
5. 3	Recommendations for Future Experimentation .....	84
<b>References .....</b>		<b>85</b>
<b>Vita.....</b>		<b>87</b>

## List of Figures

	Page
Figure 1: Replica of Ludwig Prandtl's water tunnel experiment visualizing fluid flow field in the vicinity of a wing. ....	2
Figure 2: Sample PIV vector map of vortex. ....	3
Figure 3: Basic PIV set-up and equipment (Flowmap user's guide 2002:4-1).....	8
Figure 4: Basic PIV algorithm (Flowmap user's guide 2002:4-8). ....	11
Figure 5: Basic LALLS set-up.....	13
Figure 6: Equivalent spherical model. ....	14
Figure 7: Supersonic flow geometry over a concave corner.....	20
Figure 8: Malvern Spraytec laser diffraction particle sizer with feed tube and shroud injector. ....	26
Figure 9: Supersonic wind tunnel with piping changes and injection port.....	27
Figure 10: Test section with ramp installed.....	28
Figure 11: AFIT 6 x 6 inch supersonic wind tunnel. ....	29
Figure 12: Dantec Dynamic Solo 200 laser system. ....	31
Figure 13: Test section with laser and CCD set-up. ....	32
Figure 14: Control panel for Solo 200 laser system. ....	33
Figure 15: Dantec Dynamic FlowSense 4M camera and specifications.....	34
Figure 16: Feed tube and shroud tubes. ....	36
Figure 17: T-junction purge air injector at stilling chamber injection site. ....	38
Figure 18: Percent number particle size distribution graph example. ....	39

Figure 19: Calibration image with measured scale factor. ....	40
Figure 20: Actual laser/camera trigger pulse delay measured on oscilloscope. ....	42
Figure 21: Typical images from PIV run from project 1. ....	44
Figure 22: Sample regions from image pair represented in Figure 18. ....	45
Figure 23: D[4,3], D[3,2], D[2,0] and D[1,0] for different length shroud tubes, insulated shroud tube and 0.020 inch ID feed tube. ....	47
Figure 24: Percent number diameter size data for 10 inch long 0.25 inch ID shroud with and without insulation. ....	48
Figure 25: Percent number data for different length shroud tubes. ....	49
Figure 26: D[4,3], D[3,2], D[2,0] and D[1,0] for three different ID 10 inch long shroud tubes . ....	50
Figure 27: D[4,3], D[3,2], D[2,0] and D[1,0] for two ID feed tubes with 10 inch long 0.25 inch ID shroud tube. ....	52
Figure 28: D[4,3], D[3,2], D[2,0] and D[1,0] for increasing mass flow rates of purge air co-flow, 0.030 inch ID feed, 0.25 inch ID shroud. ....	54
Figure 29: Scalar plots of U with velocity vector overlay for projects 1 and 2. ....	59
Figure 30: Normalized U scalar plot for projects 1 and 2 ( $U_{\infty} = 613.1$ m/s for project 1, 603.2 m/s for project 2). ....	60
Figure 31: Typical images from project 7. ....	61
Figure 32: Scalar plot of U with velocity vector overlay for the 6 x 6 tunnel. ....	62
Figure 33: Scalar plot of normalized U for the 6 x 6 tunnel ( $U_{\infty} = 491.7$ m/s). ....	63

Figure 34: Scalar plots of V for projects 1 and 2 with a display of theoretical shock and expansion wave locations. ....	64
Figure 35: Profile plot locations with visual shock wave location and theoretical expansion wave location. ....	65
Figure 36: Curve fits for boundary layers in projects 1 and 2 ( $U_{\infty} = 613.1$ and $603.2$ m/s respectively) with curve fit equation showing value for $\delta_2$ . ....	66
Figure 37: Curve fit for boundary layer in project 7 ( $U_{\infty} = 491.7$ m/s) with curve fit equation showing value for $\delta_2$ .....	67
Figure 38: Normal and y-component of velocity theoretical relaxation response of multiple particle diameters for project 2.....	70
Figure 39: Curve fits of relaxation time for profile 5 ( $V_n$ ), project 1 (34.4 psia) and 2 (22.6 psia) versus distance (mm) and time ( $\mu$ s).....	72
Figure 40: Typical image from project 6 (80 SLPM) and project 4 (no purge). ....	76
Figure 41: Normalized U scalar plots for projects four through six ( $U_{\infty} = 597.1, 594.3, 594.4$ and $595.1$ m/s respectively). ....	77



## **List of Tables**

	<b>Page</b>
Table 1: Feed tube and shroud combinations utilized. ....	37
Table 2: Wind tunnel projects. ....	43
Table 3: Project 1, 2, and 7 theoretical flow properties and characteristics. ....	55
Table 4: Project 3-6 theoretical flow properties and characteristics. ....	56
Table 5: Normalized velocity average and standard deviation for projects 1, 2 and 7. ....	68
Table 6: Boundary layer comparisons for projects 1 and 2. ....	69
Table 7: Particle relaxation times and diameters for projects 1-6, profiles 2-5. ....	73
Table 8: Particle diameters for profile 5, simple and Knudsen model. ....	74

# **CHARACTERIZATION AND CONTROL OF CARBON DIOXIDE SEED PARTICLES IN PARTICLE IMAGE VELOCIMETRY**

## **1. Introduction**

### **1.1 Motivation and Hypothesis**

Modern aerodynamic research possesses a myriad of theoretical and experimental techniques for obtaining a broad spectrum of information relating to fluid flows including temperature, velocity, pressure and force. Early theoretical calculations in aerodynamics utilized integral and algebraic forms of the mass, momentum and energy conservation equations singularly and simultaneously to compute fluid properties. With recent advances in computing power early theoretical computations have in a large part given way to the more advanced field and numerical methods of computational fluid dynamics (CFD). While the number and quality of CFD calculations has increased greatly since its advent, experimental wind tunnel data remains a critical analysis tool to validate theories and models, and to obtain data in regimes that have not yet been analyzed by CFD.

Experimental methods for measuring qualitative and quantitative flow field properties in a wind tunnel can be categorized as either intrusive or non-intrusive. Intrusive techniques involve the insertion of a measurement device into the fluid flow such as a probe in hot wire anemometry. Non-intrusive techniques are techniques which

do not disrupt the flow by inserting measurement devices into the fluid such as the use of pressure sensitive paint (PSP).

Particle Image Velocimetry (PIV) is a non-intrusive method for obtaining a quantitative velocity vector map for a given fluid flow field. Unlike hot wire anemometry which is a point measurement technique, PIV provides a qualitative view of an entire flow field. In 1904, Ludwig Prandtl was able to obtain a qualitative description of a fluid flow field in the vicinity of a wing by seeding water with mica particles in a human driven water tunnel as illustrated in Figure 1 (Kompenhans, 2006:8).

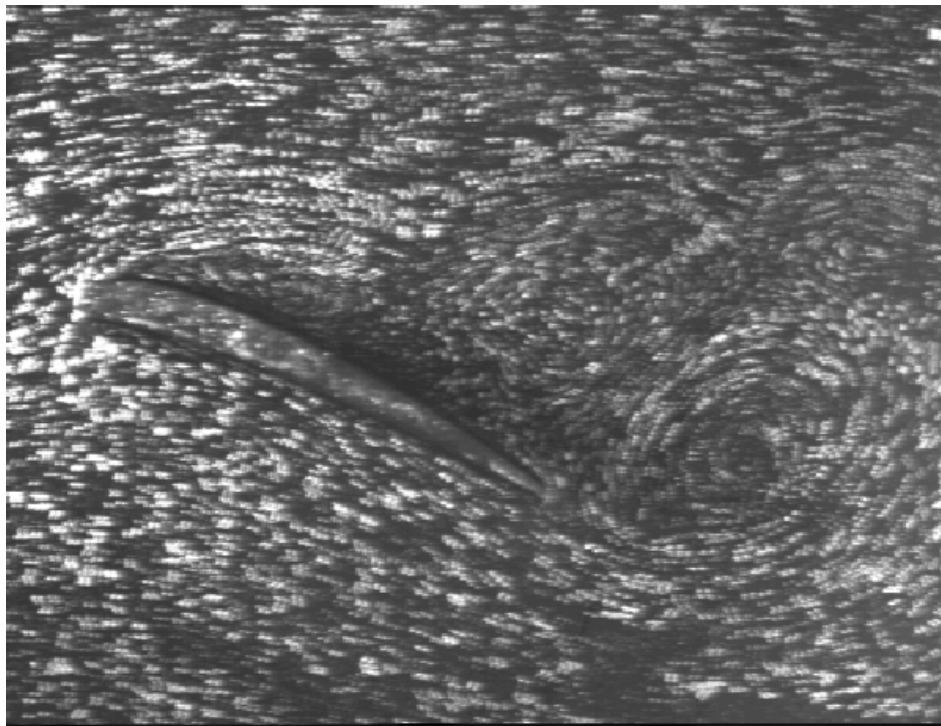


**Figure 1: Replica of Ludwig Prandtl's water tunnel experiment visualizing fluid flow field in the vicinity of a wing.**

Although only qualitative information could be extracted by Prandtl in his early experiments, the successful seeding of a fluid flow for visualization was an important

precursor in the development of PIV. The development of PIV as an experimental technique during the last 20 years allows for extraction of qualitative and quantitative information. For more information, Adrian (2005) provides an encompassing history of PIV, including a roadmap for the future. A sample PIV velocity vector map of a vortex similar to the vortices shown in Figure 1 is shown in Figure 2 (Mokry et al., 1999:300). In addition, PIV provides a means of viewing the time history of a flow field, particularly useful in the study of turbulent flows.

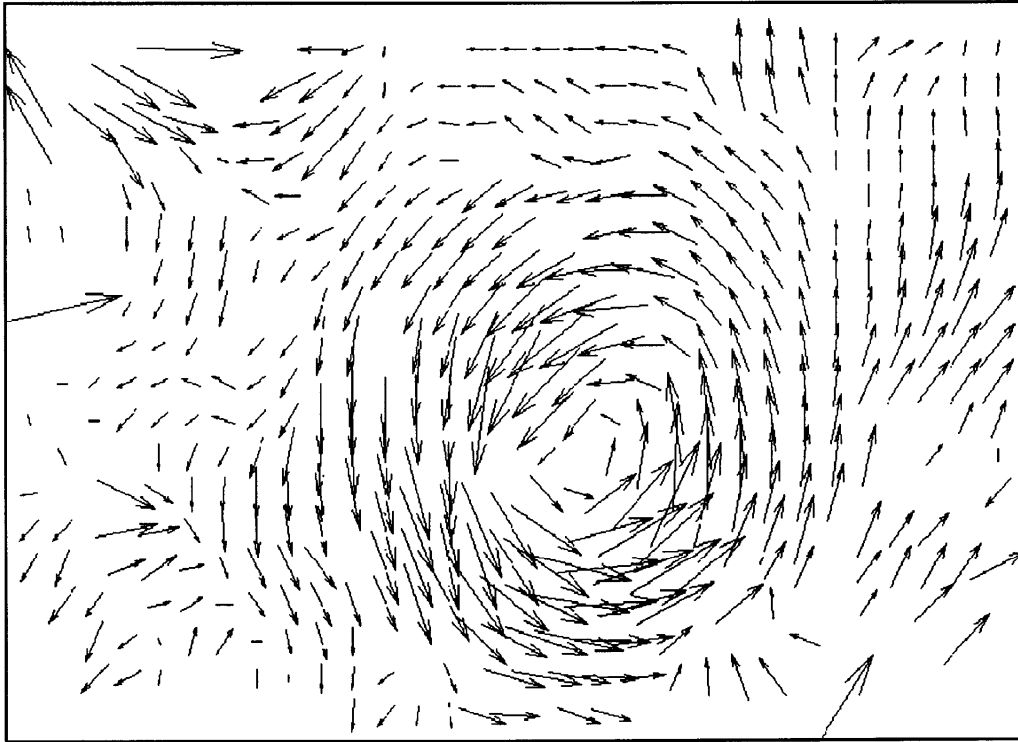


**Figure 2: Sample PIV vector map of vortex.**

Equipment requirements for PIV measurements include an illumination source, image capture device, a system to synchronize the illumination source and image capture device, and seeding material. When seed particles are illuminated, the seed particles

reflect the electromagnetic energy from the illumination source and this energy is stored by the image capture device. When two images are taken in quick succession, the particles on the resulting image pair can be correlated from one image to the next. With a sufficient number of particles and sufficient number of image pairs for statistical accuracy, these correlations provide a velocity map of the flow field through the simple computation of the distance travelled by each particle divided by the time between successive image captures shown below.

$$V_{flow} = \frac{D}{t} \quad (1)$$

Seed materials require certain properties to be effective. First, the seed must be detectable. In Prandtl's era this requirement translates to the seed material being visible to the naked eye. Today, this detection means the seed particles must be large enough to scatter sufficient electromagnetic energy from an illuminator to be detected by a charge coupled device (CCD). Secondly, the particles must be small enough to track the flow with sufficient accuracy.

Until recently, most seeding materials were persistent, that is exhibiting an inappreciable degradation once resident in the wind tunnel. The persistence of seed materials creates disadvantages for their use since the wind tunnel, models, fans, compressors and anything else the seed material comes in contact with require cleaning after each use and in extreme cases, wind tunnel equipment could even suffer damage by using the seed material. The persistence of seed materials negatively impacts experiments due to time and manpower consumed to clean equipment and also inhibits the

repeatability of any experiment. Recently, carbon dioxide in the form of solid particles has been used as a seeding material in PIV experiments. The advantage of using solid carbon dioxide particles is that the seed particles are non-persistent. After passing through the test section, a thermodynamic environment in which the solid particles do not sublime, the particles pass through the diffuser and enter a thermodynamic environment where sublimation occurs. The utilization of carbon dioxide as seeding material for PIV has been called “clean seeding” due to the quick and complete sublimation of all seeding particles. Thus, the need to clean equipment is eliminated and experiments are easily and quickly replicated making PIV a more attractive process to the aerodynamic engineer, and more importantly, the tunnel operators and technicians.

At this time, the limitations of clean seeding are still being investigated. Successful demonstrations of PIV using clean seeding in supersonic wind tunnels, prove the concept is viable, however, the fidelity of clean seeding PIV still requires investigation. Thermodynamic environments in the test sections of low speed wind tunnels typically are environments that lead to the sublimation of CO<sub>2</sub>, and this renders the CO<sub>2</sub> ineffective as a seed material. The sublimation of CO<sub>2</sub> and the thermodynamic environment of low speed wind tunnels complicate the use of clean seeding in a low speed wind tunnel as the initial particle size, the rate of change of particle size due to sublimation, residence time of particles and other factors become very important. The fact that clean seeding is a recent advancement also leads to a lack of established techniques and procedures for its implementation. The scalability and versatility of the technique must be determined to make this approach to flow seeding viable for large-scale closed circuit wind tunnels, where the clean advantages are most pronounced. Further research is required to continue

the development of clean seeding PIV as a viable and useful tool to the aerodynamic community.

## **1.2 Research Focus and Goals**

The focus of this research is the refinement of clean seeding as a viable PIV technique. Utilizing carbon dioxide as the seeding material for PIV has already been accomplished with mixed results in previous work at AFIT and the main focus of this research is the characterization of particles, to include investigating methods to control particle size. Specific objectives include the following:

- Characterize carbon dioxide particle size, absolute and relative, with respect to different diameter feed tubes and different diameter and length shroud tubes.
- Attempt to control particle size through the introduction of a purge gas to the carbon dioxide injection system.
- Utilize the characterization and control in the first two objectives to achieve successful clean seeding PIV results using the stilling chamber of the Air Force Institute of Technology (AFIT) 2.5 inch X 2.5 inch supersonic wind tunnel as the injection location.
- Characterize carbon dioxide particle size by their response time as they travel through a shock wave and compare the results to theoretical models.
- Scale up clean seeding experiments to the AFIT 6 inch X 6 inch supersonic wind tunnel.



## 2. Overview and Literature Review

### 2.1 PIV Overview

PIV is a method that measures a fluid flow field using sophisticated equipment and correlation algorithms to solve the basic equation of motion equaling distance divided by time (1). Technological advances in laser, CCD digital cameras and computers have enabled PIV to progress from a method only applied in specialized laboratories to a versatile and economically viable off-the-shelf experimental tool (Tropea et al., 2007:312). Requirements for effective PIV include an illumination source, an image capture device, imaging optics to focus the light into a thin sheet, and seed material, not to scale, as shown in Figure 3 (Flowmap user's guide 2002:4-1).

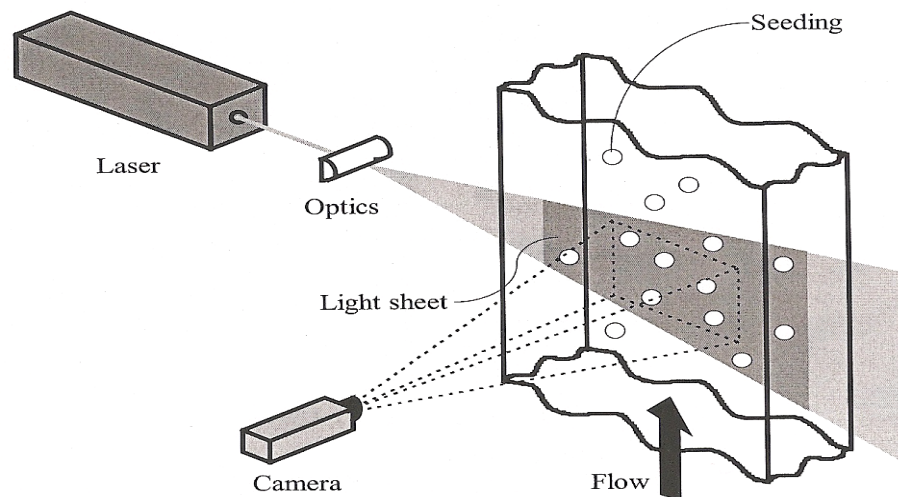


**Figure 3: Basic PIV set-up and equipment (Flowmap user's guide 2002:4-1).**

In addition to the basic equipment shown, PIV employs synchronization equipment to control the illumination and image capture devices. Computers and specifically designed software perform this synchronization and complete the data analysis making the entire process readily achievable for the PIV novice.

Illumination sources for PIV must meet three requirements (Tropea et al., 2007:313). First, the illumination pulse must be of short enough duration that the image capture of the seed material is a circular dot rather than a streak caused by the movement of the particle during illumination. For higher speed airflows, such as supersonic airflows, a laser capable of very short pulse duration is a necessity to freeze the motion of seed particles (Flowmap user's guide, 2002:3-3). Secondly, the illumination must be optically manipulated into a thin sheet in order to ensure seed particles are in focus and fixed in depth. Cylindrical and spherical lenses perform this manipulation (Tropea et al., 2007:314). Mirrors in combination with optics in devices such as light arms may increase flexibility in the positioning and orientation of the light sheet. Lastly, the illumination source must produce enough power to illuminate the seeding particles such that the image capture device is able to capture the particle illumination reflections. Flows utilizing small seed particles or PIV measurements of larger areas require a higher power output, while larger particles and smaller areas of flow can be measured with lower power illuminators.

The most common illumination device used in PIV measurements is the pulsed Neodymium-doped yttrium aluminum garnet (Nd:YAG) laser. Typical characteristics include a 10 milliJoule to 1 Joule power output with a 5-15 nanosecond pulse duration.

The major limitation for the Nd:YAG laser is the repetition rate of 10-50 Hz that limits temporal resolution. Recent developments in solid state Neodymium-doped yttrium lithium fluoride (Nd:YLF) lasers have lead to better temporal resolution with repetition rates of up to 6 kHz. This increase in temporal resolution comes at the price of an increase in pulse duration to 50-300 ns and a decrease in power to 10-40 mJ (Tropea et al., 2007:314).

Technological advances in the area of image capture devices include replacing the 35mm camera using photographic film with sophisticated digital charge coupled devices (CCDs). Further enhancements are CCDs allowing the storage of reflections from the particles on two distinct and subsequent image frames replacing CCDs storing the image pair on one frame. The result is a simplifying of the analysis by eliminating the ambiguity of which particle reflections belong to which frame in the image pair.

A myriad of PIV analysis techniques exist, but all methods are a variation on one basic correlation technique. Two image pairs are broken down into interrogation regions, typically square regions of 16x16, 32x32 or 64x64 pixels. Analysis of the interrogation regions in the frequency spectrum using fast Fourier transforms (FFT) is the first step in acquiring a full flow field vector map. Basically, an interrogation region in the first image moves pixel by pixel while comparing the correlation to the second image. A peak occurs when the interrogation region in image one matches the particle reflections with image two. Correlation in the frequency domain and conversion back into the time domain by an inverse Fourier transform provides a distance vector map of each particle's pixel movement between frames. Calibration images using known distances in the test section in comparison with camera images and pixel pitch provide the necessary scale factor to

convert this pixel distance into a test section distance. With a known delay between image captures, producing an interrogation region planar flow field velocity map is simply a matter of computing distance divided by the delay time. This process, repeated for all interrogation regions, yields a near instantaneous velocity field in the entire planar cross-section. Utilizing sophisticated filters and interrogation techniques, to include window shifting, overlapping, local averaging and sub-pixel interpolation leads to increases in accuracy and spatial resolution. The basic transformation and correlation algorithm follows in Figure 4 (Flowmap user's guide 2002:4-8)

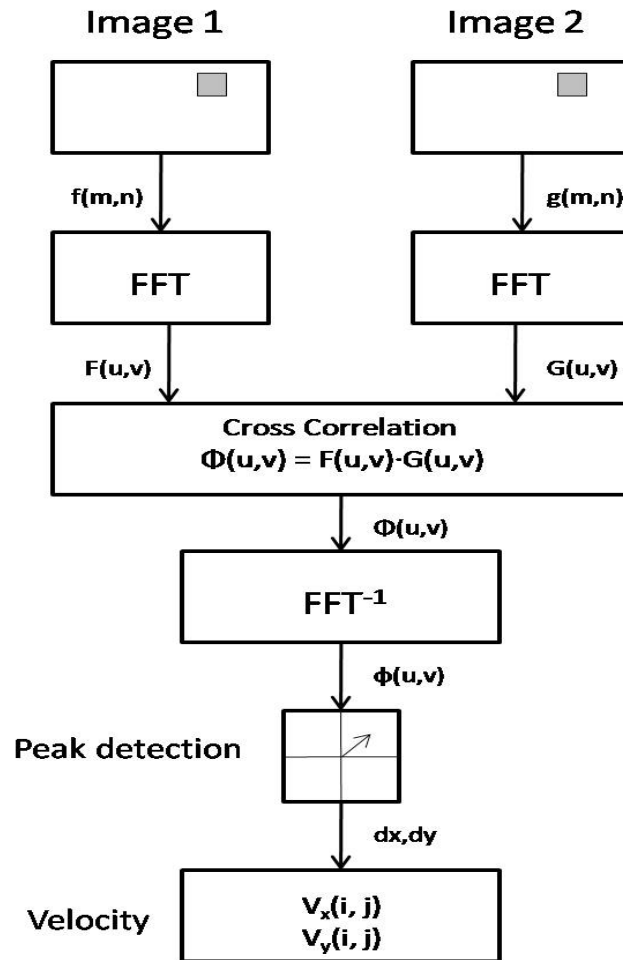


Figure 4: Basic PIV algorithm (Flowmap user's guide 2002:4-8).

Seeding for use in PIV involves balancing two restrictions; the first restriction is the seed particle must be of sufficient size to reflect enough energy from the illumination source to enabling the storage of the reflected energy on the image capture device. The second restriction is the particles be of sufficient size to accurately track the flow. In a supersonic air flow with solid particles this requirement correlates to the particles having a diameter between 0.5 and 5.0  $\mu\text{m}$  (Tropea et al., 2007:288).

## **2.2 Particle Sizing Using Laser Diffraction**

Many different methods of measuring particle size exist, from using sieves and sedimentation methods to the more sophisticated microscopy and laser diffraction techniques (Rawle, 5). The method in use in this research is laser diffraction or Low Angle Laser Light Scattering (LALLS). This methodology utilizes the Mie scattering theory that states the diffraction angle for a particle is inversely proportional to the particle size itself. The only requirements for measurements using LALLS are a source of coherent light of fixed wavelength and a suitable detector. Typical illuminators are He-Ne gas lasers with a wavelength of 0.63  $\mu\text{m}$  that demonstrate stability, especially in temperature, and a better signal to noise ratio than higher wavelength lasers. The detector is a set of individual photosensitive silicon detectors. As a particle passes through the illuminator, a lens focuses the diffracted light in order to direct the light to the detector. Measuring the location of this light on the detector provides particle size determination by Mie scattering theory computations. The process is shown in Figure 5 below

(Spraytec, 2006:2-4) showing the illuminator (1), two different particle sizes (2) reflecting light through the lens (3), and finally impacting the detector (4)

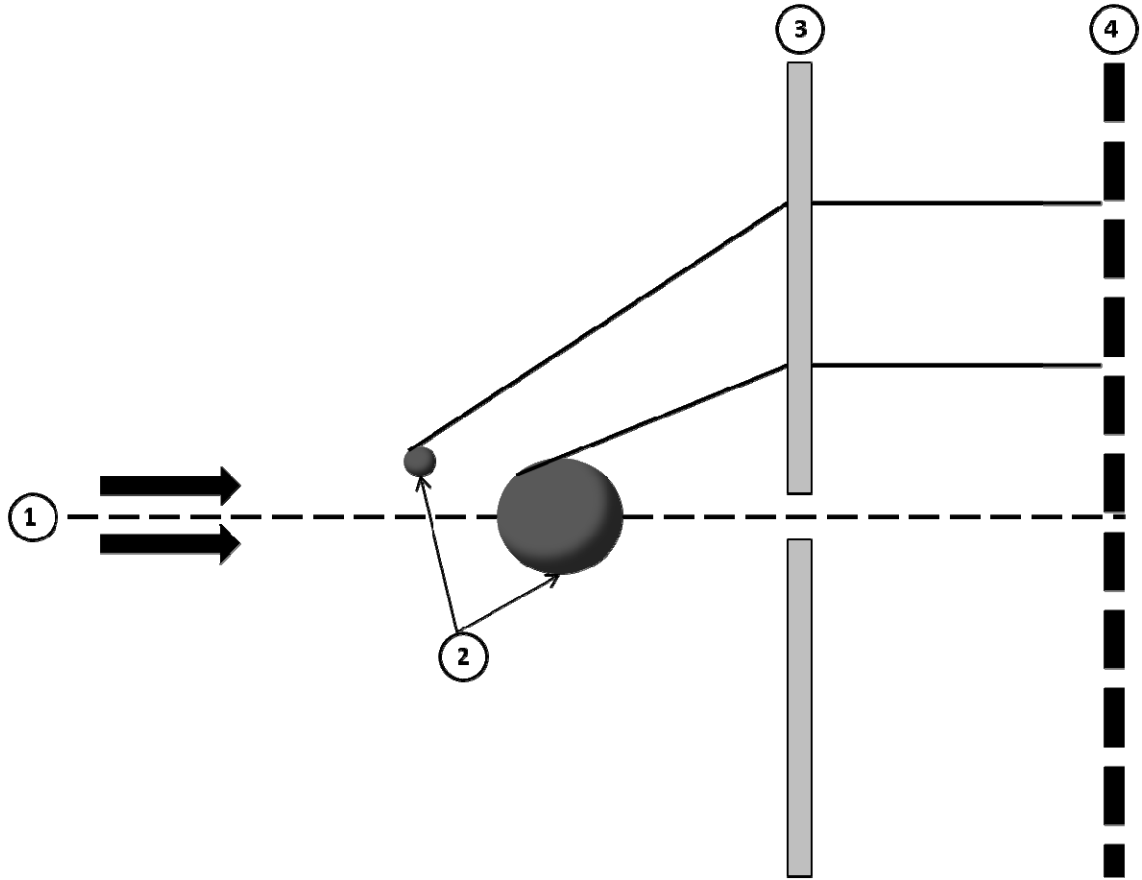


**Figure 5: Basic LALLS set-up.**

Figure 5 portrays the particles as spheres, as one Mie scattering theory assumption is that particles are spherical in shape. Since a sphere is the only volume which can be described by one dimension, the diameter, sizing of particles using an equivalent spherical model creates a standard that will not be misinterpreted in regards to the dimension intended. In LALLS particle sizes convert to spherical diameters using an equivalent volume computation. For example, a cylindrical particle of 20  $\mu\text{m}$  diameter

and 100  $\mu\text{m}$  height is equivalent in volume to a 39.15  $\mu\text{m}$  diameter sphere as shown in Figure 5.

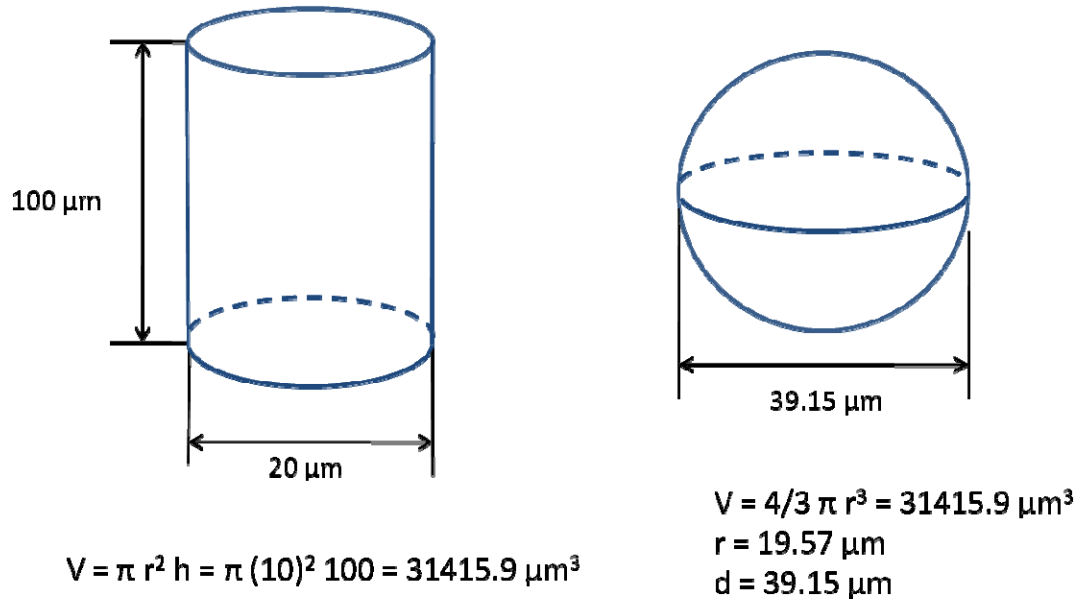


**Figure 6: Equivalent spherical model.**

Laser diffraction uses a volume based measurement to display the diameter of the particle, so the sizes reported are equivalent spherical volume diameters. In a simplified example, the particles may be cylindrical in shape identical in dimensions to the cylinder in Figure 6, but the diameter will be reported as 39.15  $\mu\text{m}$  which is the equivalent spherical diameter.

The LALLS produces a volumetric diameter, specifically  $D[4,3]$  the volume-moment mean diameter (Allen, 1990:151). In  $D[4,3]$  the initial numeral [4] indicates the diameters measured are raised to the fourth power and summed in the numerator, while the latter numeral [3] indicates the diameters are cubed and summed in the denominator. The resulting quotient yields the volume-moment mean diameter or  $D[4,3]$ . This volume

reporting (DeLapp, 2006:31) presents data that is not entirely useful for the particle sizing in relation to PIV, as the illumination scatter does not depend on the volume, but the surface area. LALLS approximates  $D[3,2]$  (sum of diameters cubed divided by the sum of the diameters squared), also known as the Sauter mean diameter or surface area-moment mean, producing a mean diameter based on surface area that is a useful dimension for PIV particle sizing purposes. Further, conversion to a number-surface area mean,  $D[2,0]$  (zero indicating number of particles in the denominator), or number-length mean,  $D[1,0]$ , using  $D[4,3]$  and  $D[3,2]$  is possible using equations (2) and (3) below where  $X_{gN}$  is the geometric number mean diameter and  $\sigma$  is the geometric standard deviation (Allen, 1990:186)

$$\ln D[4,3] = \ln X_{gN} + 3.5 \ln^2 \sigma \quad (2)$$

$$\ln D[3,2] = \ln X_{gN} + 2.5 \ln^2 \sigma \quad (3)$$

Inputs for solving for  $D[2,0]$  and  $D[1,0]$  are  $D[4,3]$  and  $D[3,2]$  from the laser diffraction measurement and approximation, and the outputs are  $X_{gN}$  and  $\sigma$ . Once  $X_{gN}$  and  $\sigma$  are known, equations (4) and (5) yield the number-surface area mean,  $D[2,0]$ , and the number-length mean,  $D[1,0]$  as follows (Allen, 1990:161)

$$\ln D[2,0] = \ln X_{gN} + \ln^2 \sigma \quad (4)$$

$$\ln D[1,0] = \ln X_{gN} + 0.5 \ln^2 \sigma \quad (5)$$



### 2.3 Particle Characterization Using PIV and Relaxation Time

The equation of motion for a spherical particle in a moving viscous fluid, originally deduced by Bassett and independently derived by Boussinesq and Oseen (BBO equation) follows (Dowdell, 1974:803):

$$\begin{aligned} \frac{4}{3}\pi a^3 \rho_p \frac{dv}{dt} = & \frac{4}{3}\pi a^3 \rho_f \frac{dV}{dt} + \frac{4}{3}\pi a^3 (\rho_p - \rho_f)g - 6\pi\mu a[(v_p - U) - \frac{1}{6}a^2\nabla^2 U] \\ & - 6\pi\mu a^2 \int_0^t \frac{d}{d\tau}[(v_p - U) - \frac{1}{6}a^2\nabla^2 U] \frac{d\tau}{\sqrt{\nu(t-\tau)}} - \frac{2}{3}\pi a^3 \frac{d}{dt}[(v_p - U) - \frac{1}{10}a^2\nabla^2 U] + L \end{aligned} \quad (6)$$

The terms on the right hand side of the equation are in order the non-inertial force, net body force, quasi-steady viscous force, time history force, added mass force and the lift force. Different forms of the equation appear in Melling (1997) and Tropea et al. (2007); approximations by Hjelmfelt and Mockros are in common use. For flows involving particles of densities much larger than the density of the fluid (on the order of  $10^3$ ) the equation simplifies to equation (7) (Melling, 1997:1408) where  $v_p$  is the particle velocity,  $U$  is the fluid velocity,

$$\frac{dv_p}{dt} = -C(v_p - U) \quad (7)$$

and

$$C = \frac{3}{4} C_D \text{Re}_p \frac{\mu}{\rho_p d_p^2} \quad (8)$$

The drag coefficient,  $C_D$ , is

$$C_D = 24/\text{Re}_p \quad (9)$$

for the *simple* approximation and

$$C_D = 24/[\text{Re}_p(1 + K_n)] \quad (10)$$

for the modified Stokes drag law incorporating the Knudsen number,  $K_n$ . The Knudsen number approximation improves accuracy when smaller particles are in the flow. The Knudsen number is defined as the mean free path,  $\lambda$ , divided by the diameter of the particle,  $d_p$ , where the mean free path is below and

$$\lambda = \frac{RT}{\sqrt{2}\pi d^2 N_A P} \quad (11)$$

where  $d$  is the molecular diameter of the individual fluid molecules and where  $N_A$  is Avogadro's number. One of the terms required for the drag coefficient is the dynamic viscosity of the fluid,  $\mu$ , which is highly dependent on temperature as seen below

$$\mu = \mu_0 \frac{(T_0 + T)}{(T + C)} \left(\frac{T_0}{T}\right)^{\frac{3}{2}} \quad (12)$$

where  $\mu_o = 18.27 \times 10^{-6}$  Pa's,  $T_o = 291.15$  K and  $C = 120$  K. The drag coefficient also requires the particle density. Many densities for solid  $\text{CO}_2$  are found in literature including  $1180 \text{ kg/m}^3$  in DeLapp (2006),  $1400 \text{ kg/m}^3$  in Kochtubajda et al. (1985), and  $1562 \text{ kg/m}^3$  in Peltier (2007). Due to the low pressures involved and the effects of agglomeration as discussed in Scarano et al. (2003:433), this research uses the lower value of  $1180 \text{ kg/m}^3$ .

For PIV, a particle's response is typically quantified by the relaxation time or relaxation distance. Relaxation time and relaxation distance are defined as the time or distance it takes the particle velocity lag,  $v_p - v_{pf}$ , to decrease by a factor of  $1/e$ , or  $0.368$ , when traversing an oblique or normal shock. Using equation (7), the relaxation time,  $\tau_p$ , is simply  $1/C$  and solving equation (7) for the relaxation time yields equations (13) and (14) for the simple model and Knudsen model respectively.

$$\tau_p = d_p^2 \frac{\rho_p}{18\mu_f} \quad (13)$$

$$\tau_p = d_p^2 \frac{\rho_p}{18\mu_f} (1 + K_n) \quad (14)$$

Solving equation (7) as a function of time for the instantaneous particle velocity,  $v_p$ , in terms of initial particle velocity,  $v_{pi}$ , yields equation (15) (Melling, 1997:1410).

$$\left| \frac{U - v_p}{U - v_{pi}} \right| = e^{-Ct} \quad (15)$$

Typically particle diameters are known for input into equation (8) and the relaxation time or  $1/C$  is the output. For this research, the particle size is treated as an unknown due to sublimation effects and the unknown residence time in the stilling chamber. A comparison of the velocity lag with the theoretical calculations using a non-linear curve fit solves for relaxation time. The relaxation time will then yield a particle diameter by solving equation (14). The goal is to utilize the laser diffraction data to choose an injector suitable for stilling chamber injection. Then, to display control over particle size, the injector will be combined with a co-flow of purge air to decrease the mean diameter particle size. By analyzing the data from the PIV runs, the different diameter particles in the LALLS experiment should have different relaxation times corresponding to the different particle diameters. Not only does this characterize the  $\text{CO}_2$  particles, it more importantly demonstrates the ability to control particle size.

Isentropic flow theory computations provide the conditions in the test section of the wind tunnel. The Mach number calculation is from equation (17) (Anderson, 2004:80) when the stagnation pressure,  $p_o$ , and test section pressure,  $p$ , are known (measured) below

$$\frac{p_o}{p} = \left(1 + \frac{\gamma-1}{2} M^2\right)^{\frac{\gamma}{\gamma-1}} \quad (17)$$

From the measurement of the stagnation chamber temperature,  $T_o$ , the speed of sound,  $a$ , calculation comes from equation (18)

$$a = \sqrt{\gamma RT} \quad (18)$$

where

$$T = T_o/[1+((\gamma-1)/2)M^2] \quad (19)$$

The velocity in the free stream calculation follows from equation (20)

$$V = Ma \quad (20)$$

Figure 7 shows the typical features of a supersonic fluid flow over a concave corner

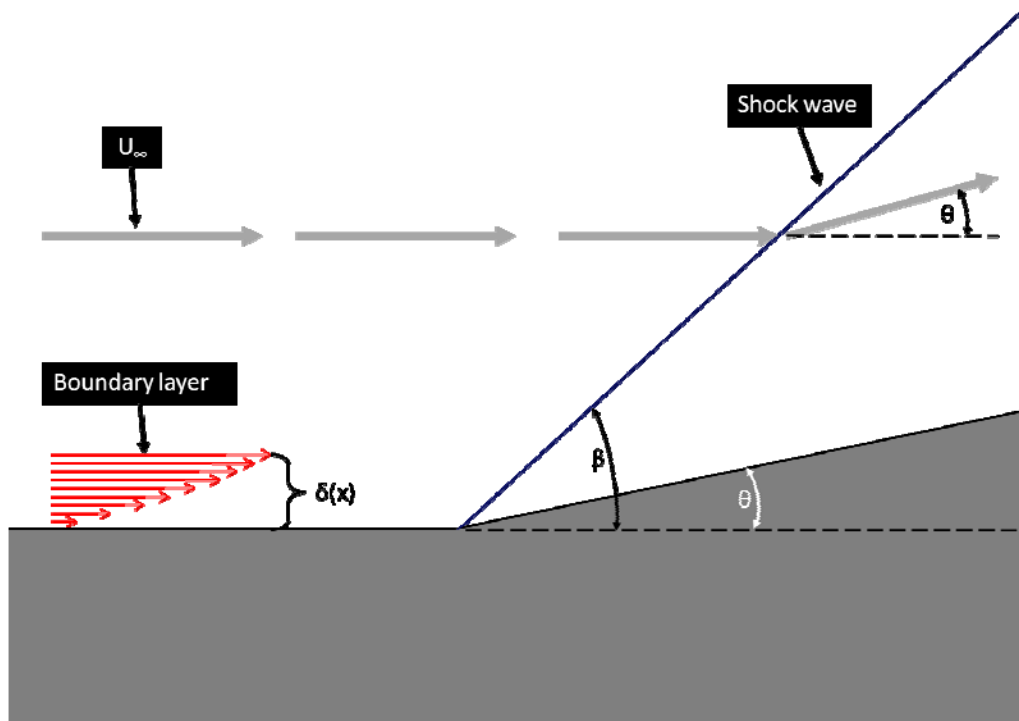


**Figure 7: Supersonic flow geometry over a concave corner**

Shown are the free stream component of velocity,  $U_\infty$ , the shock wave, and the boundary layer. Notice that the free stream component of velocity is essentially parallel to the floor of the test section, but the fluid velocity after the shock is at an angle  $\theta$  to the floor and is equal to the ramp angle. The shock angle,  $\beta$ , is calculated from the Mach number and ramp angle,  $\theta$ , from equation (16) below

$$\tan \theta = 2 \cot \beta \left[ \frac{M^2 \sin^2 \beta - 1}{M^2 (\gamma + \cos 2\beta) + 2} \right] \quad (21)$$

where  $M$  is the free stream Mach number. The shock angle  $\beta$  is used to calculate the normal component of the upstream shock,  $M_{n1}$ , in turn used to compute the normal component of the downstream shock using equations (22) and (23) respectively

$$M_{n1} = M \sin \beta \quad (22)$$

$$M_{n2} = \sqrt{\frac{M_{n1}^2 + [2/(\gamma - 1)]}{[2\gamma/(\gamma - 1)]M_{n1}^2 - 1}} \quad (23)$$

The last step in calculating velocities beyond the shock is to calculate temperature after the shock,  $T_2$ , using the isentropic equation

$$T_2 = T_1 \left[ 1 + \frac{2\gamma}{\gamma + 1} (M_{n1}^2 - 1) \right] \left[ \frac{2 + (\gamma - 1)M_{n1}^2}{(\gamma + 1)M_{n1}^2} \right] \quad (24)$$

In a fluid flow the boundary layer, or the layer of reduced velocity immediately adjacent to the surface past which the fluid is flowing, is difficult to quantify, especially in a turbulent flow. According to theory, the thickness of this layer,  $\delta(x)$ , is the height of the flow that is 99% or less of the free stream velocity flow. One empirical model for the calculation of the thickness of a turbulent boundary layer over a flat plate is

$$\delta(x) = 0.37x\left(\frac{U_{\infty}x}{\nu}\right)^{-\frac{1}{5}} \quad (22)$$

where  $x$  is the horizontal distance the turbulent fluid travels over the flat plate,  $U_{\infty}$  is the free stream velocity and  $\nu$  is the kinematic viscosity (Schlichting, 1968:638). Additionally, Schlichting (1968) contains two empirical models for a compressible boundary layer relating the normalized velocity distribution,  $\frac{U}{U_{\infty}}$ , to the distance above the flat plate,  $y$ , divided by the momentum thickness,  $\delta_2$ , and displacement thickness,  $\delta_1$ , respectively in equations (23) and (24).

$$\frac{U}{U_{\infty}} = 0.683\left(\frac{y}{\delta_2}\right)^{1/7} \quad (23)$$

$$\frac{U}{U_{\infty}} = 0.737\left(\frac{y}{\delta_1}\right)^{0.1315} \quad (24)$$

In a turbulent compressible boundary layer, the ratio of the boundary layer thickness to momentum thickness is equal to  $72/7$  and the ratio of the boundary layer thickness to the displacement thickness is equal to 8 or

$$\delta = \frac{72}{7} \delta_2 \quad (25)$$

$$\delta = 8\delta_1 \quad (26)$$

## 2.4 Recent Research and Literature

Although PIV is utilized in a variety of different fluid applications, the fluid flow in this research refers to a supersonic flow of air in a wind tunnel. For extensive study of compressible, or supersonic, flow theory the reader is referred to *Modern Compressible Flow* by Anderson (2003), specifically one dimensional isentropic flow in chapter three, and oblique shock and expansion wave theory in chapter four. For a more detailed description of PIV, including particle characterization, the reader is referred to the *Springer Handbook of Experimental Fluid Mechanics* edited by Tropea et al., Yarin and Foss (2007) and *Particle Image Velocimetry, a Practical Guide* by Raffel (1998). Melling (1997) and Scarano et al. (2003) are critical reads for a more detailed discussion on particle characterization and response relating to relaxation time. Peltier (2007) provides a succinct and concise overview of compressible flow theory in his paper *Performing Particle Image Velocimetry in a Supersonic Wind Tunnel Using Carbon Dioxide as the Seed Material*. In addition, Peltier (2007) analyzes wind tunnel theory and provides a detailed description of the wind tunnel and associated Labview control software utilized in this experiment. Improvements to the wind tunnel and control program have been made and are covered in chapter three.



Clean seeding research is progressing in recent years from a proof of concept toward a viable technique. Research by DeLapp (2006) provides an initial particle sizing analysis using the same laser diffraction instrument as this research. DeLapp utilizes three different nozzles and feed tubes to characterize particle size and perform an analysis of the sublimation rate of the particles exiting the injection apparatus. DeLapp also performed a comparison of theoretical CO<sub>2</sub> particle relaxation time to theoretical TiO<sub>2</sub> relaxation time, and finally performed a proof of concept for clean seeding PIV in a supersonic wind tunnel.

McNiel continued the research into clean seeding by investigating two injection sites with various injection devices. Both McNiel and DeLapp attempted clean seeding PIV by injecting CO<sub>2</sub> into the stagnation chamber, but both results produced a condensate, or fog, of particles too small to be effectively utilized for PIV. Both achieved moderate success utilizing an injection port located just upstream of the nozzle. McNiel also examined the use of a multi-port injector as well as an injector consisting of a feed tube followed by a larger diameter shroud tube. Finally, McNiel demonstrated the addition of CO<sub>2</sub> had an insignificant impact on the specific heat ratio, and thus, the Mach number and velocity produced in the wind tunnel.

Peltier continued to investigate the feed tube and shroud combination injection system with a variety of injection sites to include the nozzle, stagnation chamber, a cavity located in the test section and through a cone model inserted into the test section. Similar results to McNiel and DeLapp were obtained when attempting injection into the stagnation chamber.

### **3. Methodology**

#### **3.1 Experimental Apparatus and Setup**

##### *3.1.1 Malvern Spraytec System Set-up and Procedure*

One of the goals of this research was to apply clean seeding by injecting CO<sub>2</sub> into the stilling chamber of the wind tunnel in order to avoid the potential flow disruption caused by injecting in close proximity to the nozzle of the wind tunnel. Based on the previous attempts at stilling chamber injection, the particle size entering the test section of the wind tunnel was too small due to sublimation and produced a fog in the test section unsuitable for PIV application. In order to use the stilling chamber as an injection source, larger particles needed to be introduced. Therefore, measurements by a laser diffraction device were utilized in order to acquire trends in particle size in relation to several variables. The techniques used to attempt to change and quantify the size of particles included varying feed tubes diameters, shroud tubes diameters and lengths, using co-flow purge air and insulating the shroud tube. All of these methods were measured by a Malvern Spraytec laser diffraction particle sizing device identical to the device utilized by DeLapp (2006). The set-up is shown in Figure 8, where the distance from particle exit to the laser was held constant at three inches.

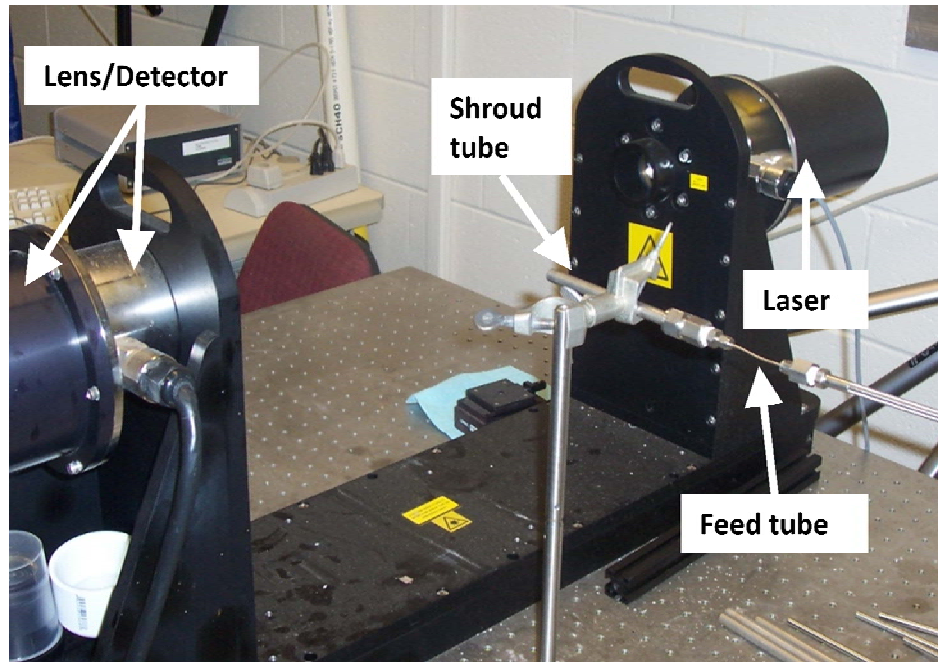


**Figure 8: Malvern Spraytec laser diffraction particle sizer with feed tube and shroud injector.**

### *3. 1. 2 Wind tunnel set-up.*

The wind tunnel is an open circuit blow down wind tunnel with a Mach 3 nozzle. The wind tunnel is identical to the tunnel used by Peltier (2007) except for some replacements in piping pictured below in Figure 9.

**Figure 9: Supersonic wind tunnel with piping changes and injection port.**

Peltier (2007) provides a detailed description of the wind tunnel to include the Leslie valve, solenoid valve and tunnel characteristics. The injection port is on the top of the stilling chamber shown in Figure 9 and the injection devices vary in regards to feed tube and shroud tube combinations. The ramp is a 10 degree ramp as measured by an inclinometer, pictured in the test section in Figure 10 below.

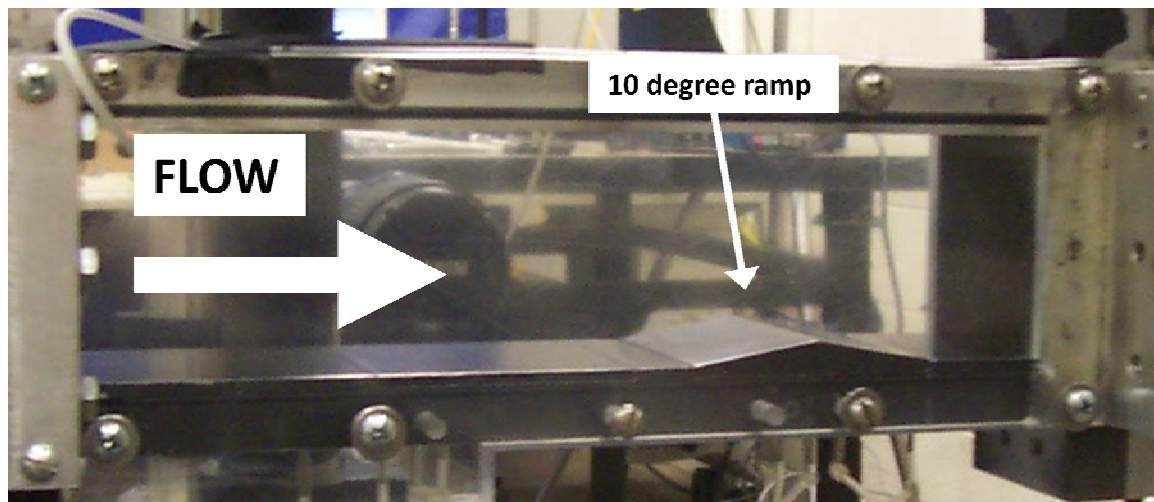


**Figure 10: Test section with ramp installed.**

A Labview program utilized and presented by Peltier (2007) controls the wind tunnel solenoid valves for the vacuum and high pressure air source. The program also creates a log of the control and vacuum pressures as well as the measured pressures in the stilling chamber and test section throughout the run. One significant improvement to the program is the addition of a temperature log for the thermocouple in the stilling chamber at the location shown in Figure 8. Due to the data acquisition (DAQ) board in use, the first addition required the input of a cold junction constant (CJC) to obtain accurate temperatures. This first attempt displayed a plus or minus 5 degree K temperature variance at a constant temperature attributable to noise in the DAQ board. Further upgrades include a National Instrument USB board with CJC compensation built in that demonstrates a much more stable temperature reading (plus or minus 0.2 degrees K).

The AFIT 6 x 6 inch open circuit blow down wind tunnel provides a ready wind tunnel to accomplish a proof of concept in a larger wind tunnel. This wind tunnel is much larger with a stagnation chamber volume of approximately 23,053 in<sup>2</sup> as compared to

4,593 in<sup>2</sup> for the 2.5 x 2.5 inch wind tunnel, a ratio of five to one. The nozzle produces a supersonic flow with a Mach number of two. A mass flow rate calculation similar to McNeil (2007:91) yields a mass flow rate of air of 7.84 kg/s for the 6 x 6 inch tunnel versus 0.63 kg/s for the 2.5 x 2.5 inch tunnel, a ratio of 12.4 to 1. A picture of the 6 x 6 inch wind tunnel is shown in Figure 11 with injection ports in the stagnation chamber.

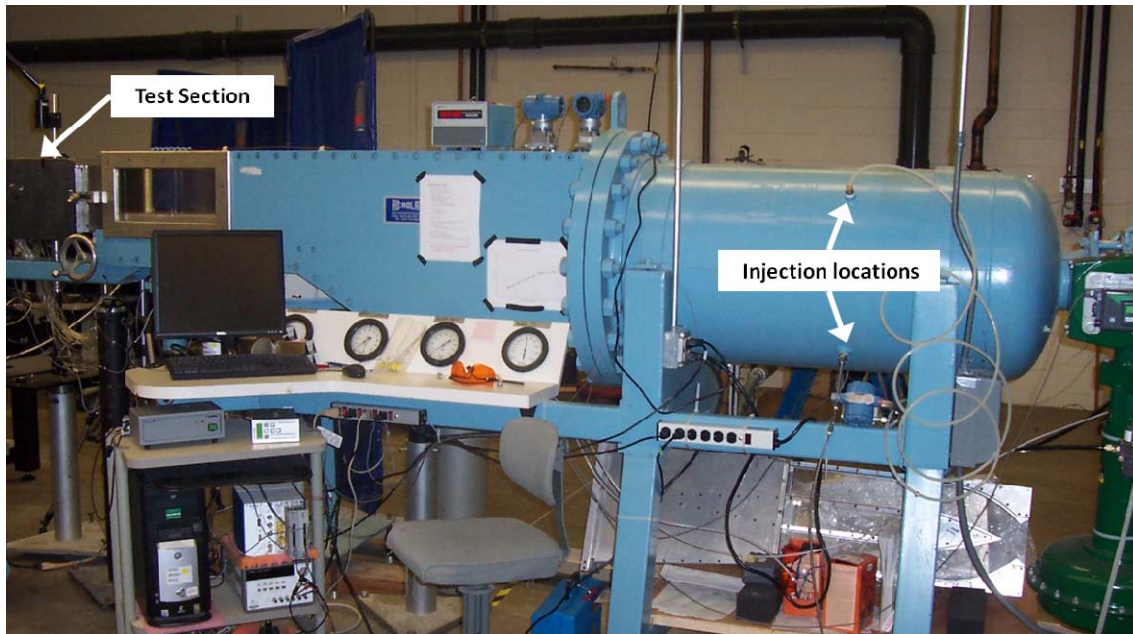


**Figure 11: AFIT 6 x 6 inch supersonic wind tunnel.**

### *3. 1. 3 PIV set up*

The PIV system is a Dantec Dynamics off the shelf PIV system including a Nd:yag pulsed laser, 2 CCD cameras, optical mirror arm, synchronization hub and controlling software. Simplifying the set-up, only one CCD camera is necessary as the

low through the test section in Figure 10 is essentially a two-dimensional flow not requiring a three-dimensional velocity vector field.

The laser system utilized was upgraded from the New Wave Research Solo 120XT laser system utilized by Peltier (2007) to the New Wave Research Solo 200XT laser system. Major differences include a larger power output (200 mJ vice 120 mJ) and an increase in power consumption (1500 watts vice 1000 watts). In addition to the laser and laser control unit, the system includes an optical arm utilized to position the laser. This optical arm was used to position the laser to provide a vertical sheet over the 10 degree ramp in the longitudinal center of the 2.5 x 2.5 inch wind tunnel. The set-up and simulated laser sheet are depicted in Figure 12.



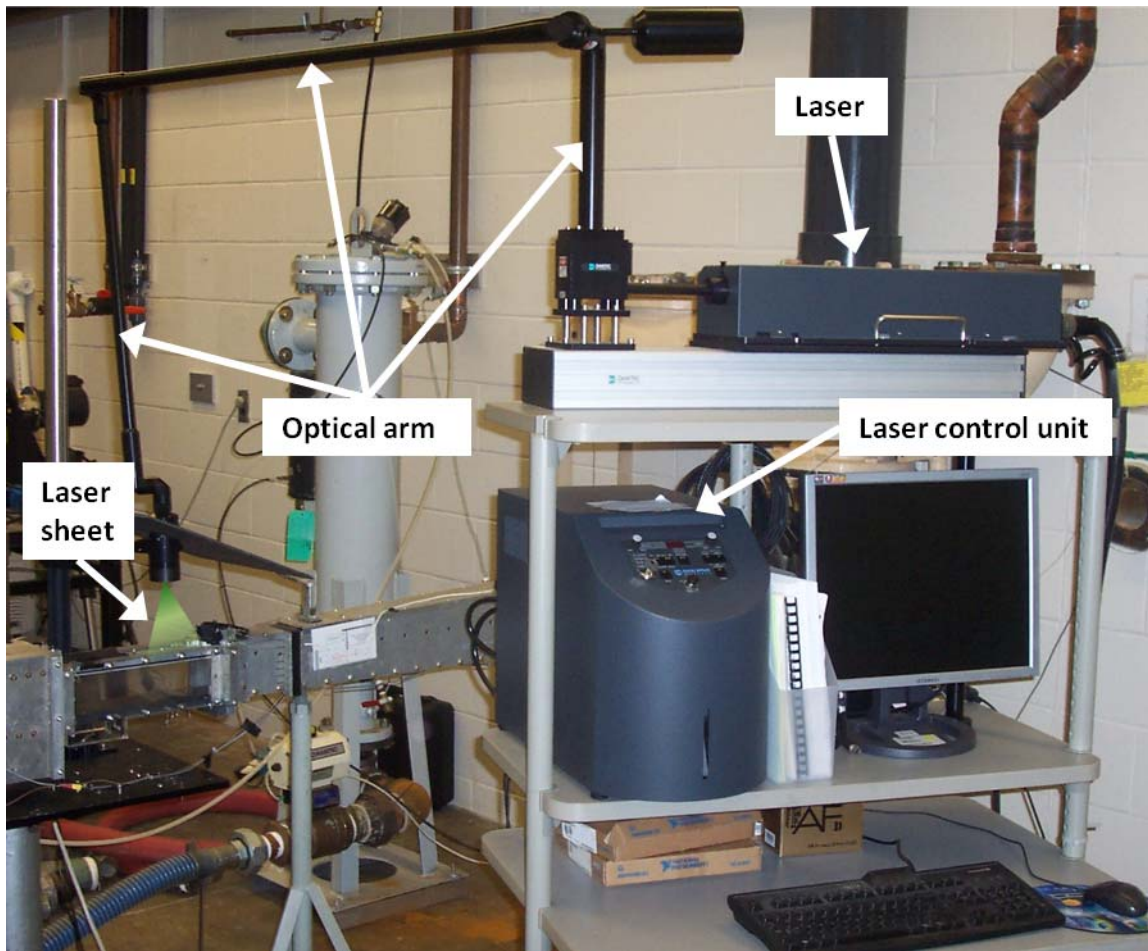


**Figure 12: Dantec Dynamic Solo 200 laser system.**

Figure 13 shows the test section, laser and CCD set-up for the AFIT 6 x 6 inch wind tunnel.



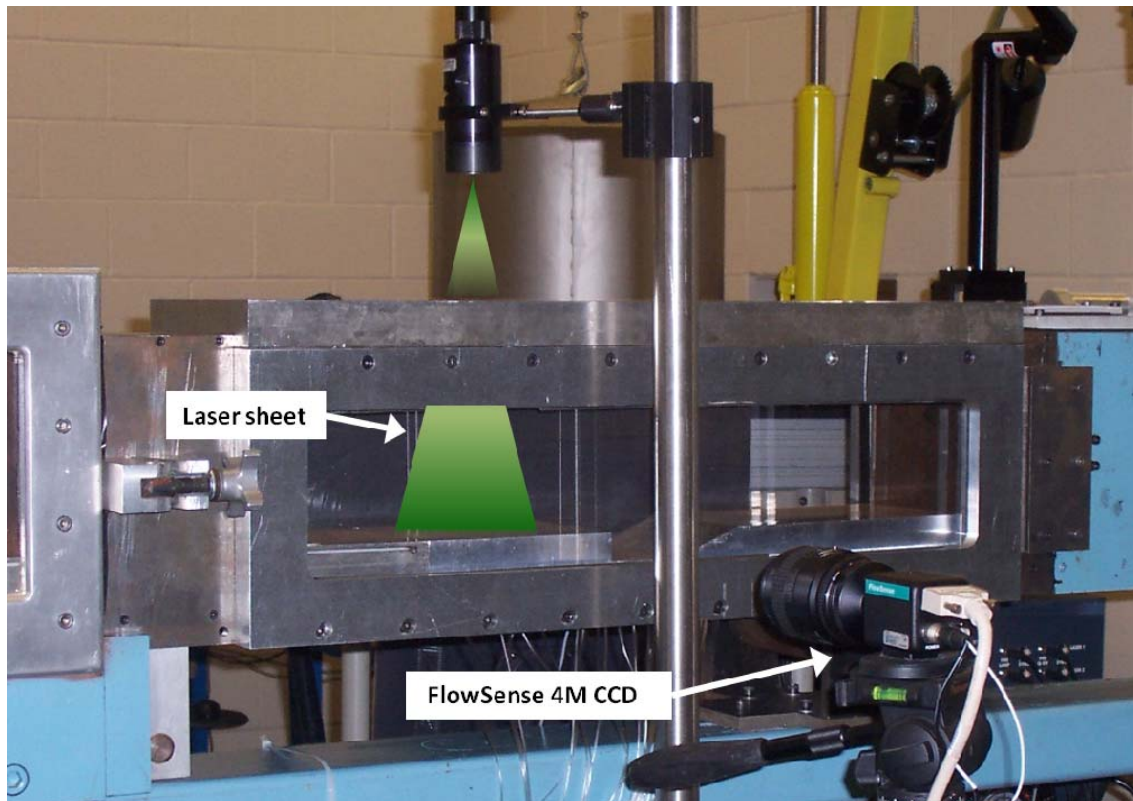


**Figure 13: Test section with laser and CCD set-up.**

The most significant improvement is a rheostat type control to vary power output pictured in Figure 14, replacing the two position toggle switch for power (high/low).



**Figure 14: Control panel for Solo 200 laser system.**

This vast improvement in power output control provides a means to more precisely control the illumination reflections from the particles and to decrease or prevent pixel saturation without using filters. For all tests in this research the power setting is 250 on high, corresponding to a 25% power output.

The camera is a Dantec Dynamics FlowSense 4M CCD camera shown in Figure 15 along with the camera's specifications.

<b>Dimensions (LxWxH)</b>	<b>85x51x51mm</b>
<b>CCD type</b>	<b>C-mount</b>
<b>Active pixels</b>	<b>2048x2048</b>
<b>Camera bit resolution</b>	<b>8, 10 or 12-bit mode</b>
<b>Pixel pitch</b>	<b>7.4 x 7.4 <math>\mu\text{m}</math></b>
<b>Signal to noise</b>	<b>&gt; 48 dB</b>
<b>Pixel clock rate</b>	<b>40 MHz</b>
<b>Max single-frame rate</b>	<b>14.5 Hz full frame.</b>
<b>PIV correlation mode</b>	<b>Yes</b>
<b>Pulse interval range</b>	<b>&lt; 1.0 <math>\mu\text{s}</math></b>
<b>Double frame rate</b>	<b>7.25 Hz full frame, 10-bit</b>

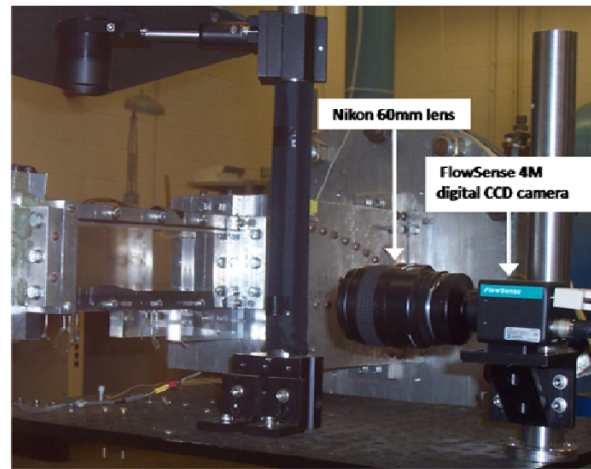


**Figure 15: Dantec Dynamic FlowSense 4M camera and specifications.**

This camera provides a critical upgrade to the research accomplished by Peltier (2007), in particular the Kodak Redlake MegaPlus Model ES 4.0/E camera utilized. As noted by Peltier, the minimum transfer pulse width recommended with the Kodak is 12 ms whereas the pixel clock rate highlighted in Table 1 for the FlowSense is less than 1  $\mu\text{s}$ . The f-stop setting for all runs is 4 and the time between pulses or frames was set at 0.4  $\mu\text{s}$ . The double frame rate for all runs is 7.4 Hz, above the maximum 7.25 Hz listed, as partial frames are used.

The controlling software for the Dantec PIV system was upgraded from the FlowManager utilized by Peltier (2007) to the Dantec Dynamic Studio software. The change in software has no significant impact on data collection or analysis. The Labview program controlling the wind tunnel also provides the external five volt trigger for the PIV system at a specified time delay. By starting the tunnel with the high pressure air and vacuum solenoids opening at set times, and by starting the PIV system with the external

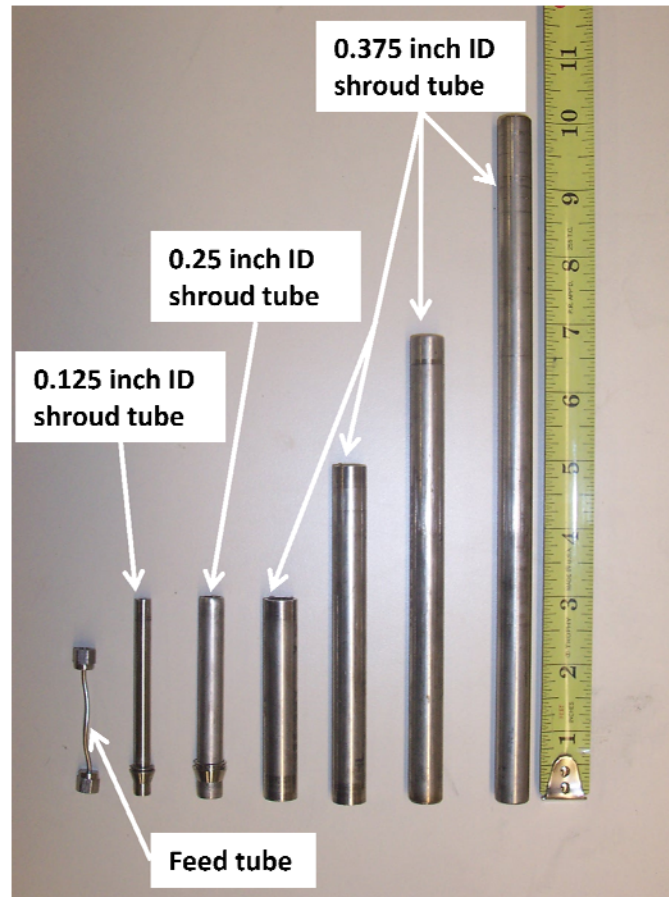
trigger at a set time after tunnel equilibrium is reached, the PIV data collection is repeated at near identical conditions.

## **3.2 Experimental Procedure**

### *3.2.1 Malvern testing*

The Malvern particle sizing environment does not replicate the environment of the intended injection site. The Malvern test environment is at atmospheric pressure in humid air whereas the stilling chamber is an environment of conditioned dry air at various higher pressures. As such, the sizing results are not an absolute result directly transferrable to the wind tunnel for PIV. The value of the particle sizing comes in the form of a trend in relative sizes. It provides the method to increase or decrease relative particle size to improve the results in the wind tunnel.

The feed tube, of which three different inner diameters (ID) were used to include 0.015, 0.020 and 0.030 inches, is shown in Figure 16. Also shown are the different size shroud tubes with IDs of 0.125, 0.25 and 0.375 inches, and lengths of three, five, seven and ten inches. A shroud length of twenty inches was also tested by putting two ten inch shrouds in series.



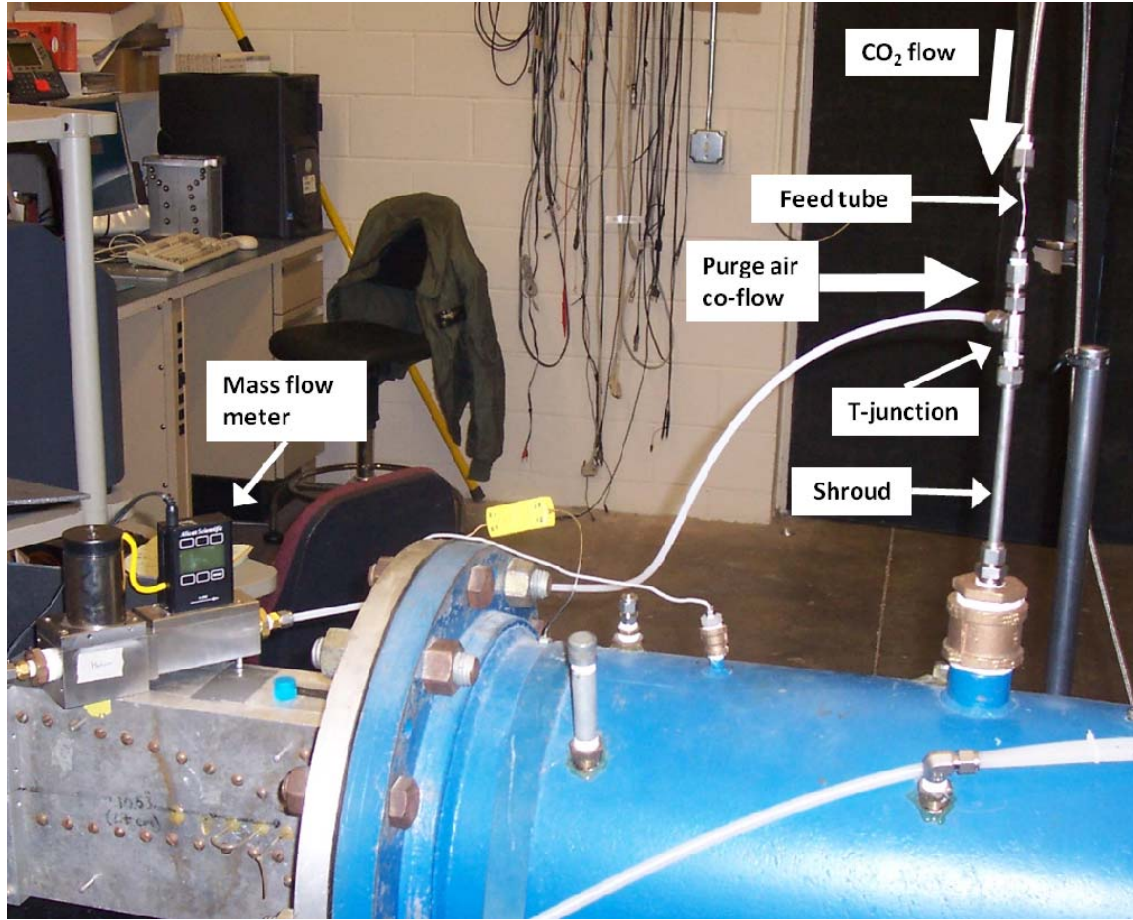
**Figure 16: Feed tube and shroud tubes.**

Table 1 shows the different combinations of feed tube and shroud tubes with the test combinations highlighted. The ten inch long 0.030 ID feed with 0.25 inch ID shroud was also tested with and without an Armaflex insulation sleeve of 0.375 inches thick covering the shroud tube. Following the initial tests, the 0.030 inch ID feed tube with 0.25 inch ID shroud tube injector was connected to a T-junction in order to measure the size of particles exiting the injector when combined with different volumetric flow rates of conditioned (dry) air. Figure 17 shows the purge air injection device inserted into the stilling chamber of the wind tunnel.



**Table 1: Feed tube and shroud combinations utilized.**

	<u>Feed Tubes</u>		
<u>Shroud Tubes</u>	0.015 inch ID	0.020 inch ID	0.030 inch ID
0.125 ID, 3 inches	X	X	X
0.125 ID, 5 inches			
0.125 ID, 7 inches			
0.125 ID, 10 inches			X
0.125 ID, 20 inches			
0.25 ID, 3 inches			X
0.25 ID, 5 inches			X
0.25 ID, 7 inches			X
0.25 ID, 10 inches	X	X	(Insulated/Purge air)
0.25 ID, 20 inches			X
0.375 ID, 3 inches			
0.375 ID, 5 inches			
0.375 ID, 7 inches			
0.375 ID, 10 inches			X
0.375 ID, 20 inches			



**Figure 17: T-junction purge air injector at stilling chamber injection site.**

For each test, the  $\text{CO}_2$  flow of approximately ten seconds of continuous measurement exhibits particle size invariance with respect to time. The ten second sample is then averaged using the provided software and the resulting output includes an averaged  $D[4,3]$  and  $D[3,2]$  with standard deviations, an averaged volumetric distribution bar graph, averaged raw percent number data as well as many other user defined variables. The  $D[4,3]$  and  $D[3,2]$  means convert the geometric number mean and standard deviation to a  $D[2,0]$  and  $D[1,0]$  mean by using equations (2) through (5). The percent

number raw data provides a useful pictorial representation of the distribution, an example of which is shown in Figure 18.

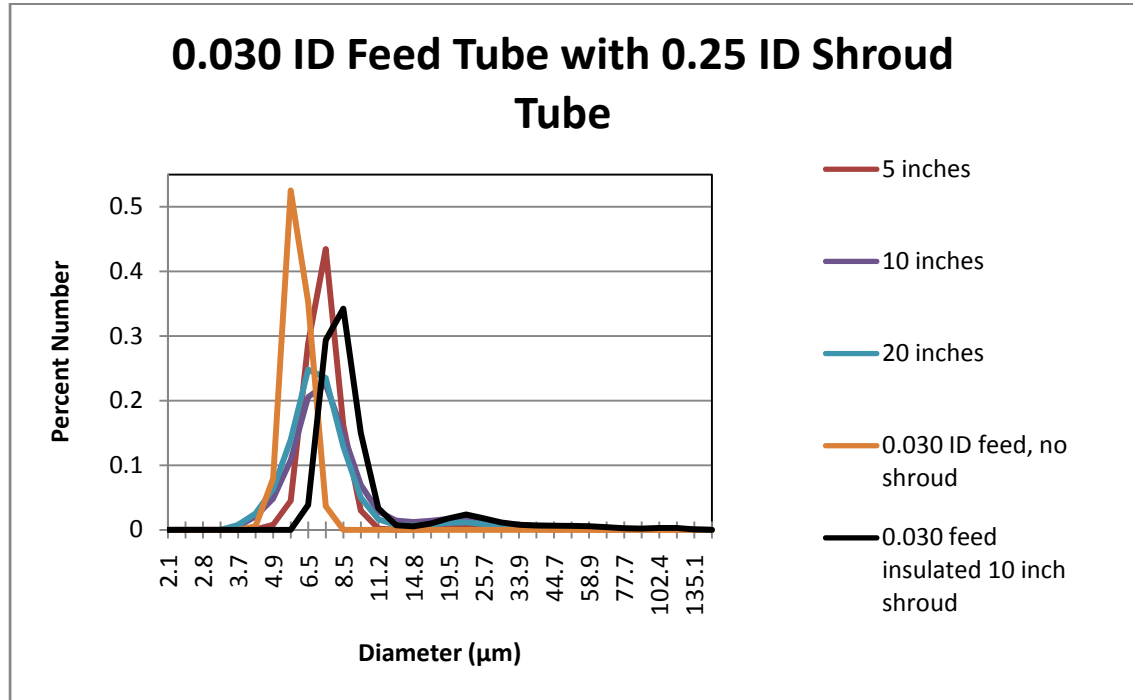


**Figure 18: Percent number particle size distribution graph example.**

### 3. 2. 2 *PIV runs*

Before actual PIV testing began in the wind tunnel, a calibration image provides a scale factor in order to convert distance in the test section to pixel distance for the camera frame. The scale factor of 5.063, equivalent to the ratio between the distances in the test section to the pixel pitch, is shown with the calibration image in Figure 19.





**Figure 19: Calibration image with measured scale factor.**

Since pixel pitch from Figure 13 is  $7.4 \times 7.4 \mu\text{m}$ , then each pixel is equivalent to a  $37.46 \mu\text{m}$ , or  $0.03746 \text{ mm}$ , distance in the test section. Furthermore, a typical  $32 \times 32$  pixel interrogation region corresponds to a  $1.20 \text{ mm}$  square area in the test section. As evident by the reverse image numbers in Figure 19, the image shown is horizontally mirrored. If not, the camera placement shown in Figure 15 would produce an image and vector map flowing right to left. Fluid flow from right to left is opposite the operator's viewpoint in Figure 13 of a left to right flow field. By horizontally mirroring the image before testing begins a more natural left to right flow is preserved throughout the PIV analysis process.

Initial runs with a 7 degree ramp, 0.020 ID feed tube with a 10 inch long 0.25 inch ID shroud tube produce results favorable for effective PIV. The particles provide more than adequate reflection and seeding density is adequate. Initial comparisons of free stream velocity with theoretical isentropic velocities, however, demonstrate a significant difference. The velocities calculated in the free stream by the PIV system are consistently 10% higher than those calculated by isentropic flow theory using the pressures and temperatures measured in the tunnel. After troubleshooting the tunnel, to include pressure transducers and the PIV system, the pulse delay sent to the laser and camera was found to not match the 0.4  $\mu\text{s}$  set in the system. After measuring the pulses on an oscilloscope there was found to be a constant positive 0.05  $\mu\text{s}$  offset for the pulses, in this case an actual pulse delay of 0.45  $\mu\text{s}$  as shown in Figure 20. The incorrect pulse delay used in velocity calculations gave consistently high velocities throughout the research that had to be corrected in the analysis by multiplying all velocities by 88.88 percent.

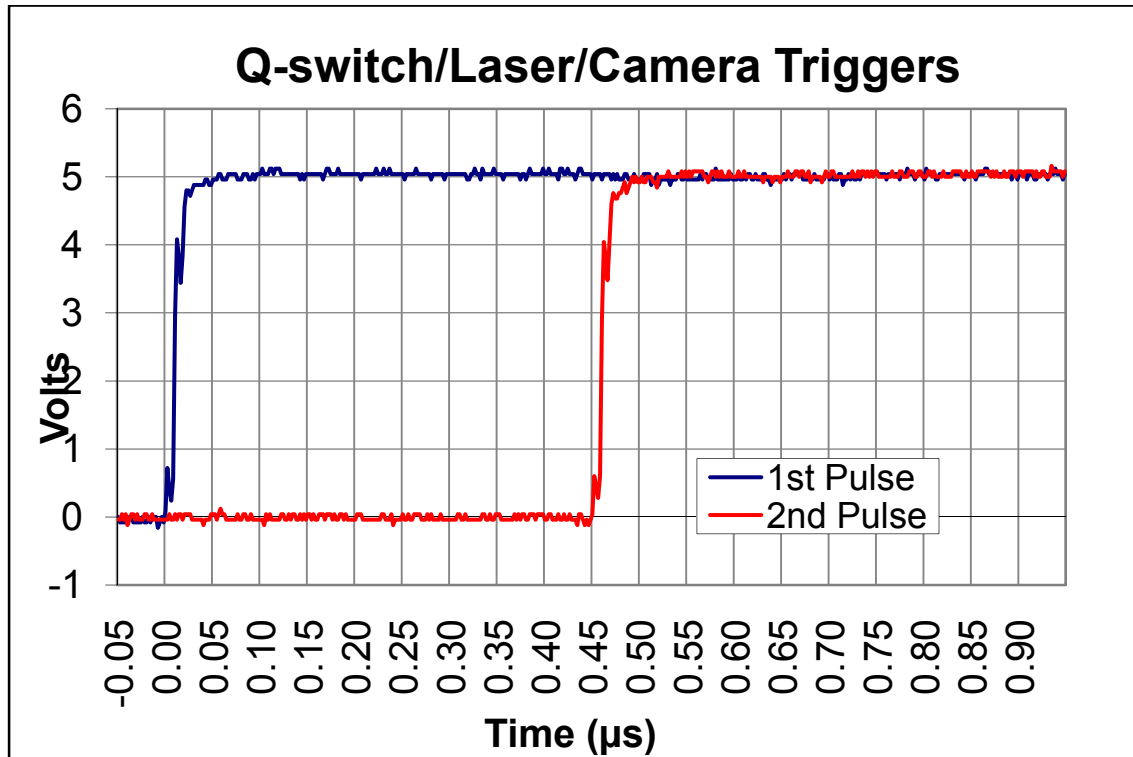


**Figure 20: Actual laser/camera trigger pulse delay measured on oscilloscope.**

To ensure adequate seeding by increasing the mass flow rate of CO<sub>2</sub> thereby ensuring fidelity through the shock, the decision was made to utilize the 0.030 feed tube. Subsequent tests all use the 0.030 inch ID feed tube with the 0.25 inch ID shroud tube. In order to increase the shock angle and the magnitudes of the velocity changes through the shock, the decision to switch to a 10 degree ramp was also made at this time.

Typical wind tunnel runs produced 50 image pairs for analysis. Multiple runs at the same settings were collected into projects for analysis. The tests projects are listed in Table 2 with control pressures, purge air use and the number of image pairs taken.

**Table 2: Wind tunnel projects.**

<b><u>Test Project</u></b>	<b><u>Control Pressure (psig)</u></b>	<b><u>Purge Air (SLPM)</u></b>	<b><u>Image Pairs</u></b>
<b>1</b>	34.4	0	500
<b>2</b>	22.6	0	503
<b>3</b>	35.4	0	100
<b>4</b>	24.7	20	100
<b>5</b>	24.8	40	100
<b>6</b>	24.8	80	100
<b>7 (6x6)</b>	24.8	0	199

Test project two utilizes the feed/shroud injector shown in Figure 8, while test project three utilizes the purge air injector pictured in Figure 17. The purge air injector was used without purge air in order to provide a baseline, or control, for the rest of the purge air projects. Project seven is the scale up of the research applying clean seeding to the 6 x 6 AFIT wind tunnel.

Interesting effects of using CO<sub>2</sub> reveal the characteristics of supersonic flow over a concave corner in a typical PIV images from the flow field shown in Figure 21.

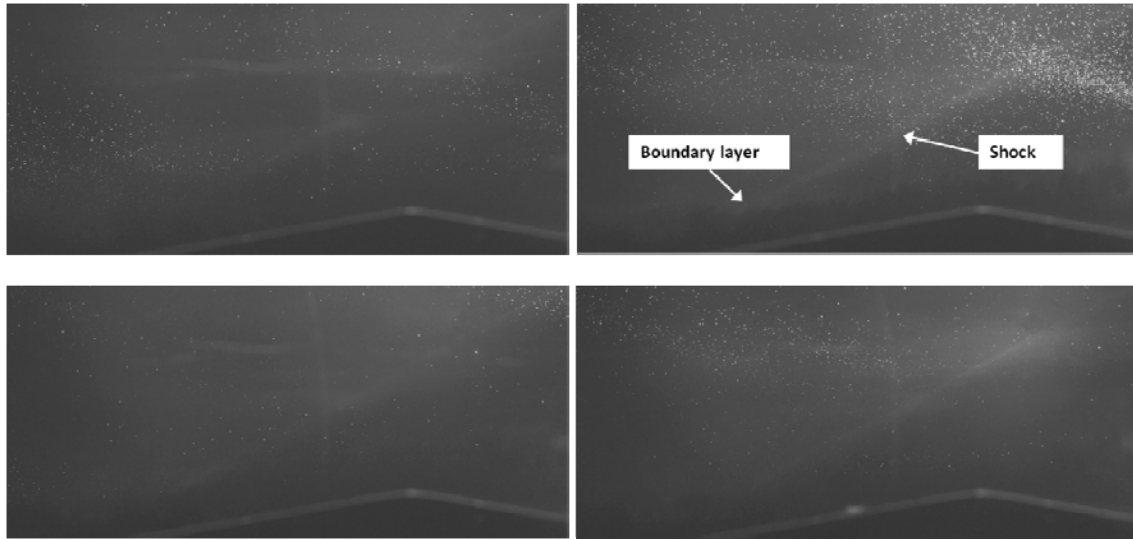


**Figure 21: Typical images from PIV run from project 1.**

Notice the boundary layer is shown as an area in close proximity to the bottom of the test section free from condensate, a characteristic of CO<sub>2</sub> condensate first shown by Miles et al. (1995). Also, the shock wave is clearly evident as a bright straight line through the condensate. The condensate, previously sublimated CO<sub>2</sub> particles encountering the much lower temperatures of the test section and reverting back to solid form, does not provide useful particles for PIV processing, but is of use for flow visualization. The particles themselves can be seen with a good dispersion throughout the images. Figure 22 displays a magnification of an image pair with a sample interrogation region of 3.75 mm x 3.75 mm.

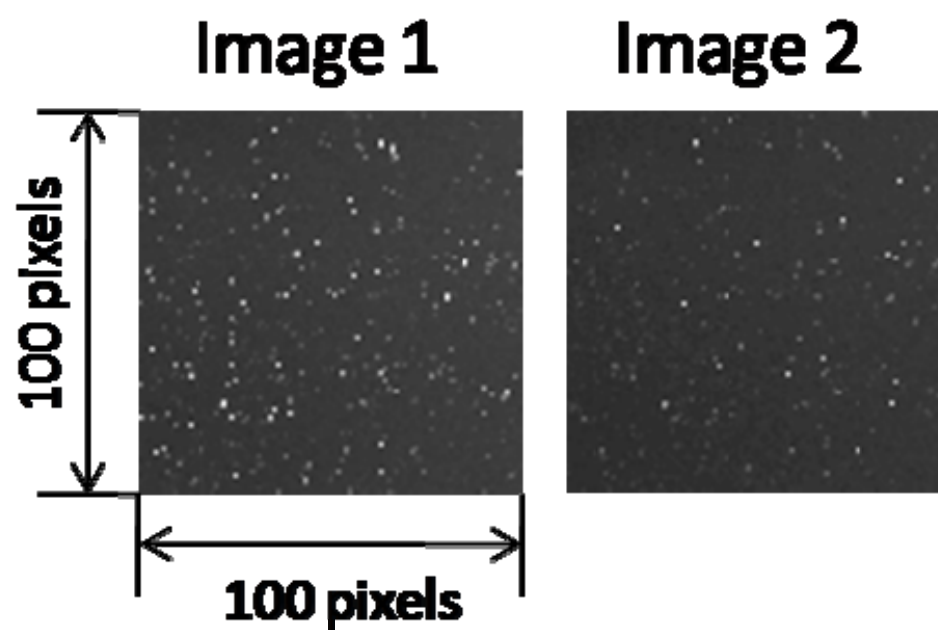
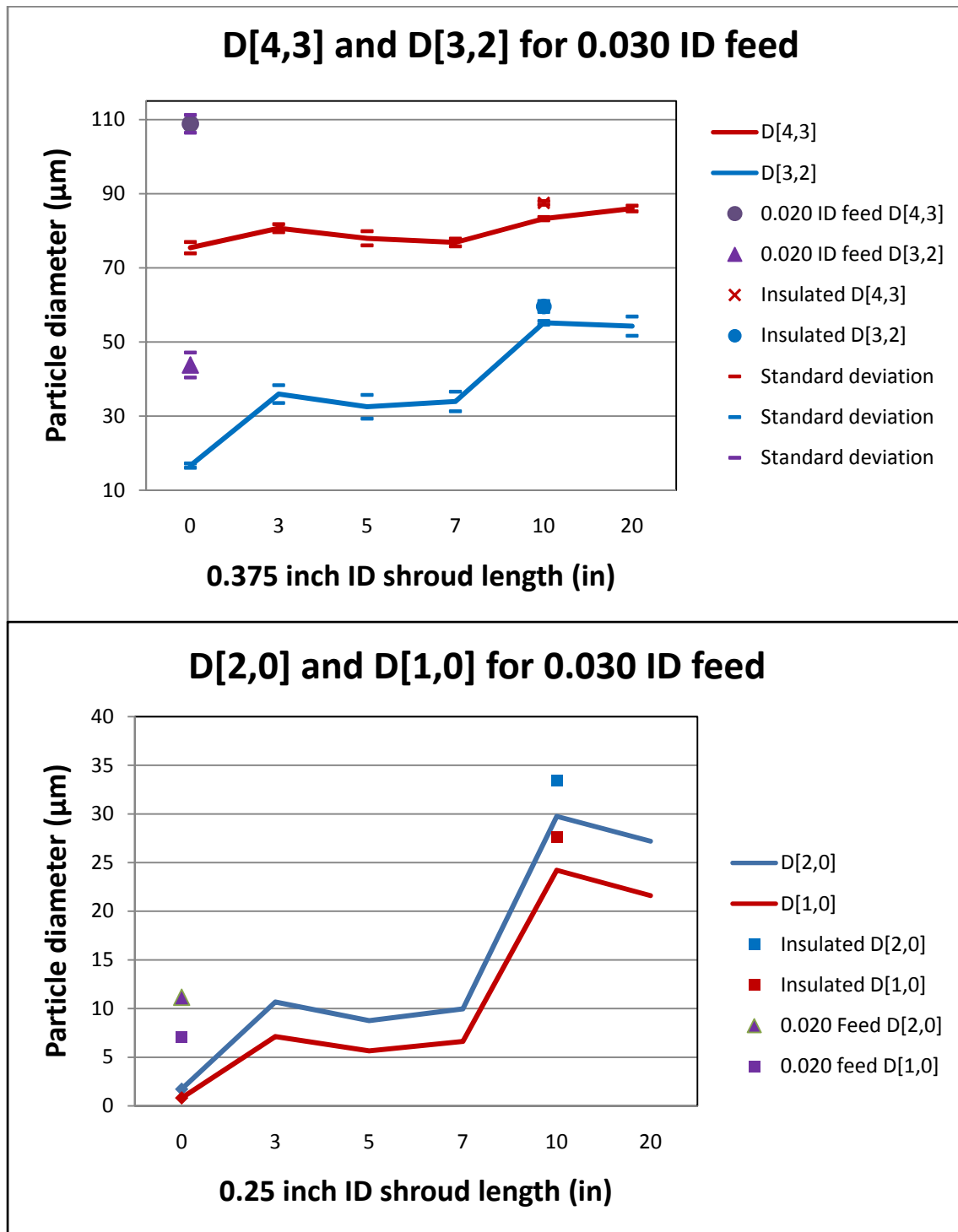


Figure 22: Sample regions from image pair represented in Figure 18.

## **4. Results and Analysis**

### **4.1 Malvern Particle Size Characterization**

An analysis of the particle sizing data reveals many trends for controlling particle size. The 0.030 inch ID feed and the 0.25 inch ID shroud comprise the baseline injector, and the tests center on this configuration as shown previously in Table 1. Figure 23 shows the results of changing shroud length from zero to 20 inches in length, and also displays the effects of insulating the 10 inch long shroud. Also shown are the means for the 0.020 inch ID feed tube without shroud.



**Figure 23: D[4,3], D[3,2], D[2,0] and D[1,0] for different length shroud tubes, insulated shroud tube and 0.020 inch ID feed tube.**



The D[4,3] results are shown as a comparison to the D[3,2], D[2,0] and D[1,0]. In all cases the D[3,2] results mirror the results of the D[2,0] and D[1,0] results on a larger scale. This is not the case for the D[4,3] results. An increase in shroud length corresponds to an increase in mean particle size until an optimum size is reached and the particle size plateaus as described by Swain et al. (Swain et al., 2007:13). Also notice the 0.020 feed with no shroud produces larger particles than the 0.030 feed with no shroud. The effects of insulating the shroud tube are obvious as the mean particle diameter increases significantly as shown in Figure 23 with confirmation in Figure 24 showing raw percent number data below

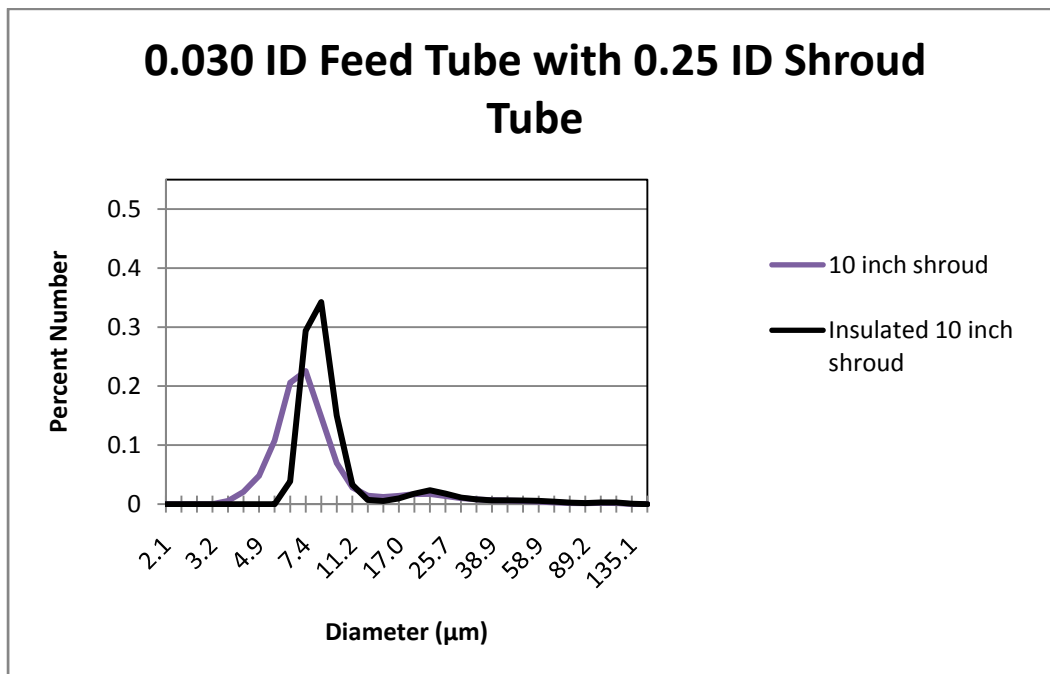


**Figure 24: Percent number diameter size data for 10 inch long 0.25 inch ID shroud with and without insulation.**

Analyzing the raw percent number data also confirms the above results pertaining to increasing particle size by using shrouds of increasing length, but also reveals the addition of a shroud tube increases the dispersion of the particle diameters as shown by the decrease in peak height and increase in peak width in Figure 25.

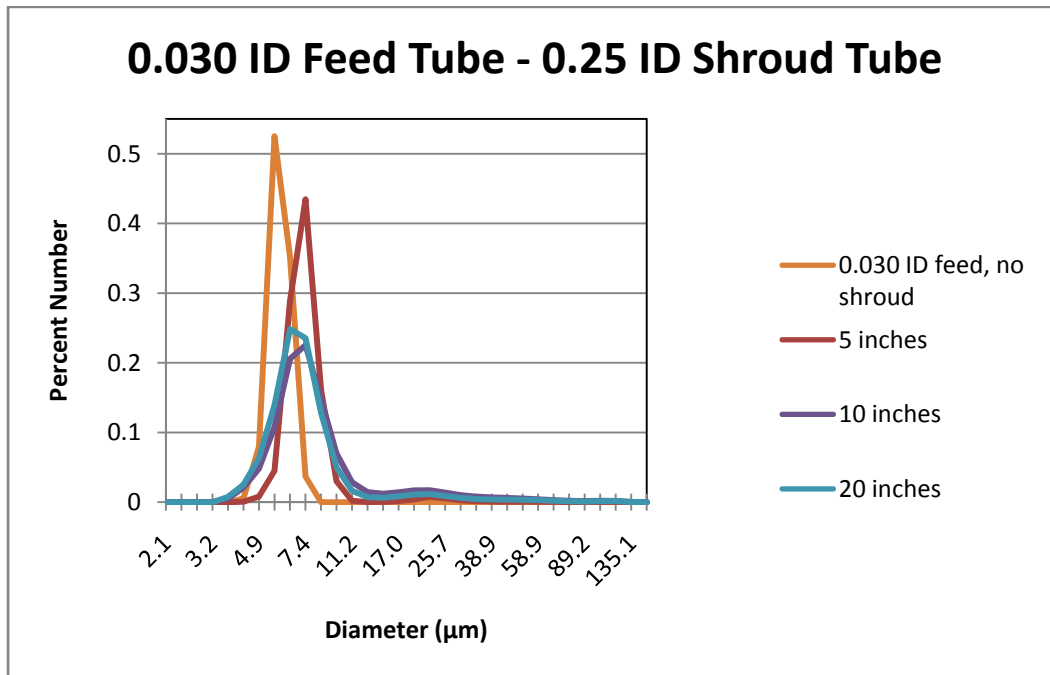


**Figure 25: Percent number data for different length shroud tubes.**

In addition to the effects of varying the length of the shroud tubes, different ID shroud tubes display noticeable trends in particle sizing as well. Figure 26 reveals increasing the shroud ID increases the mean particle diameters.

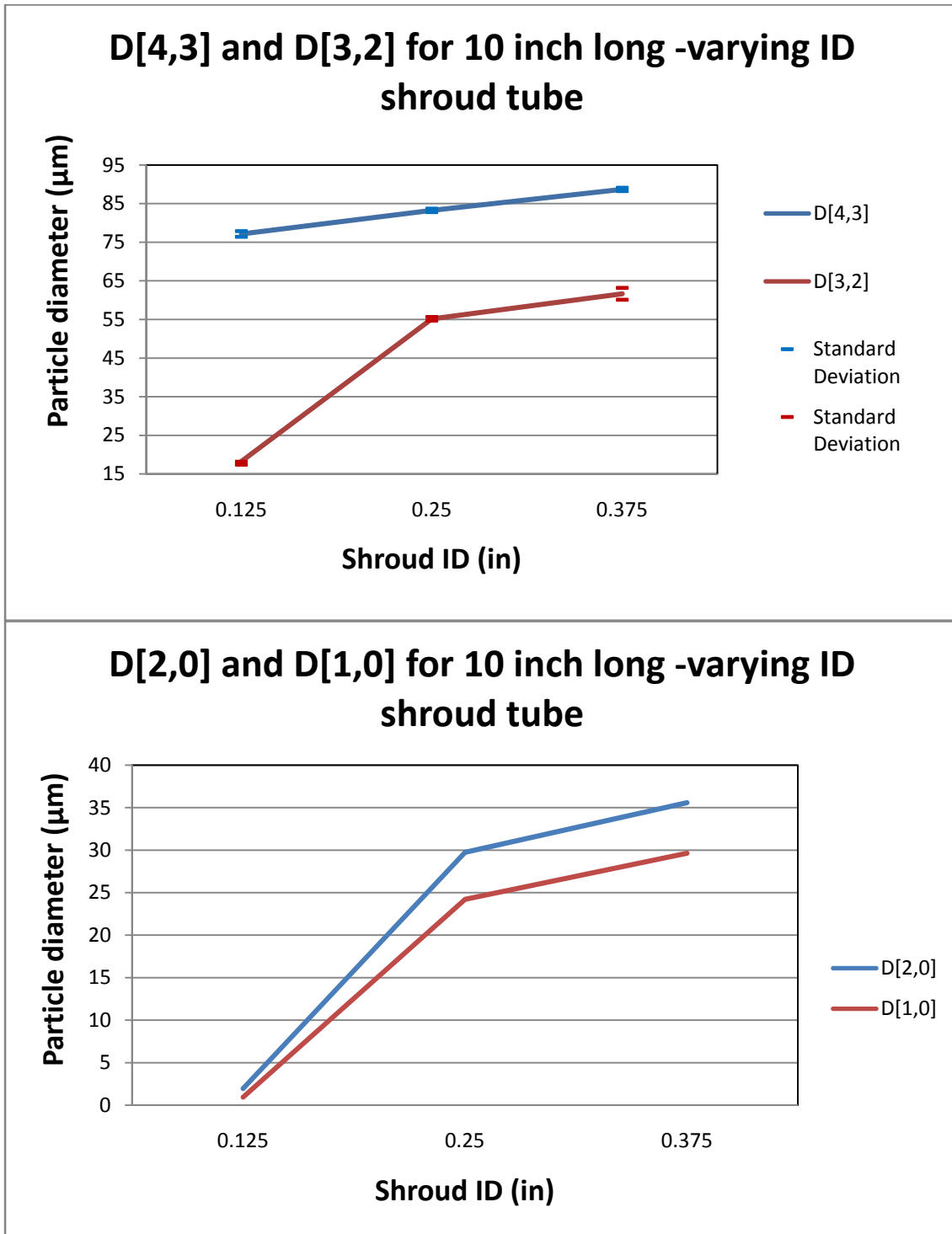


**Figure 26: D[4,3], D[3,2], D[2,0] and D[1,0] for three different ID 10 inch long shroud tubes .**

The percent raw number data results (not shown) also confirm another increase in dispersion with an increase in shroud ID. The increase in particle diameter for increasing ID of the shroud is shown particularly when progressing from the 0.125 inch ID to the 0.25 inch ID shroud tube. Peltier (2007) uses a 0.125 inch ID shroud possibly accounting for the lack of particles when injecting into the stilling chamber of the 2.5 x 2.5 inch tunnel, while this research achieves successful seeding using the 0.25 inch ID shroud.

The 0.015 inch ID feed tube exhibits an erratic and inconsistent flow rate producing inconsistent particle diameter results. Visually, the 0.015 inch ID feed produces a larger particle than the 0.020 and 0.030 inch ID feed tubes, continuing the trend shown below in Figure 27. The effect of increasing particle size by increasing the feed tube ID is first shown in Figure 23 with no shroud tube attachment, and Figure 27 confirms the trend with a 10 inch long 0.25 inch ID shroud attachment. Percent raw number data (not shown) shows dispersion increases slightly with an increase in feed tube ID.

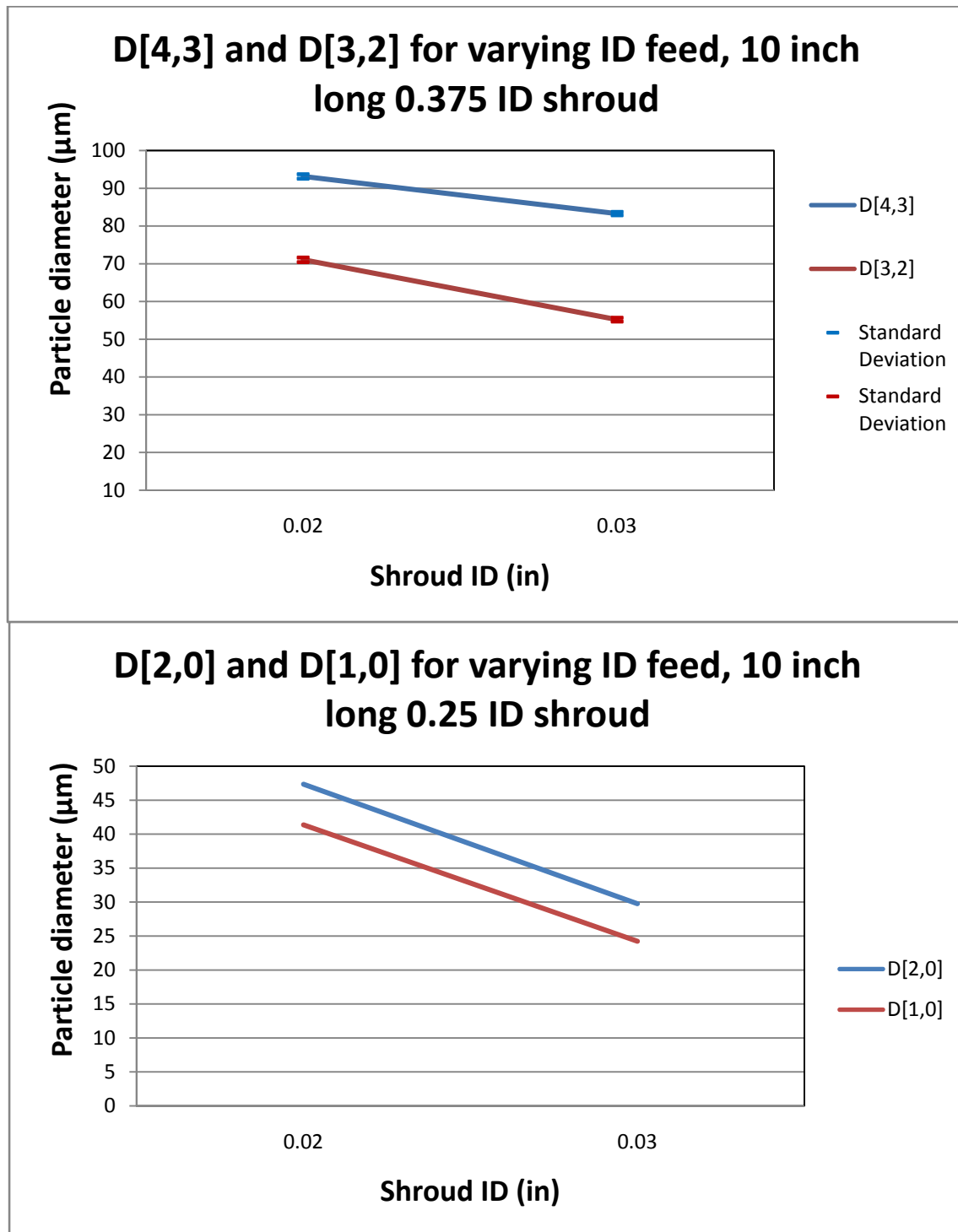


**Figure 27: D[4,3], D[3,2], D[2,0] and D[1,0] for two ID feed tubes with 10 inch long 0.25 inch ID shroud tube.**

The final analysis yields a promising rudimentary control to particle size by introducing a co-flow of purge air into the shroud tube. By increasing the flow of purge air, particle size correspondingly decreases as shown in Figure 28. Additionally, the dispersion of particle diameters remains relatively constant with the addition of purge air when examining the raw percent number data.

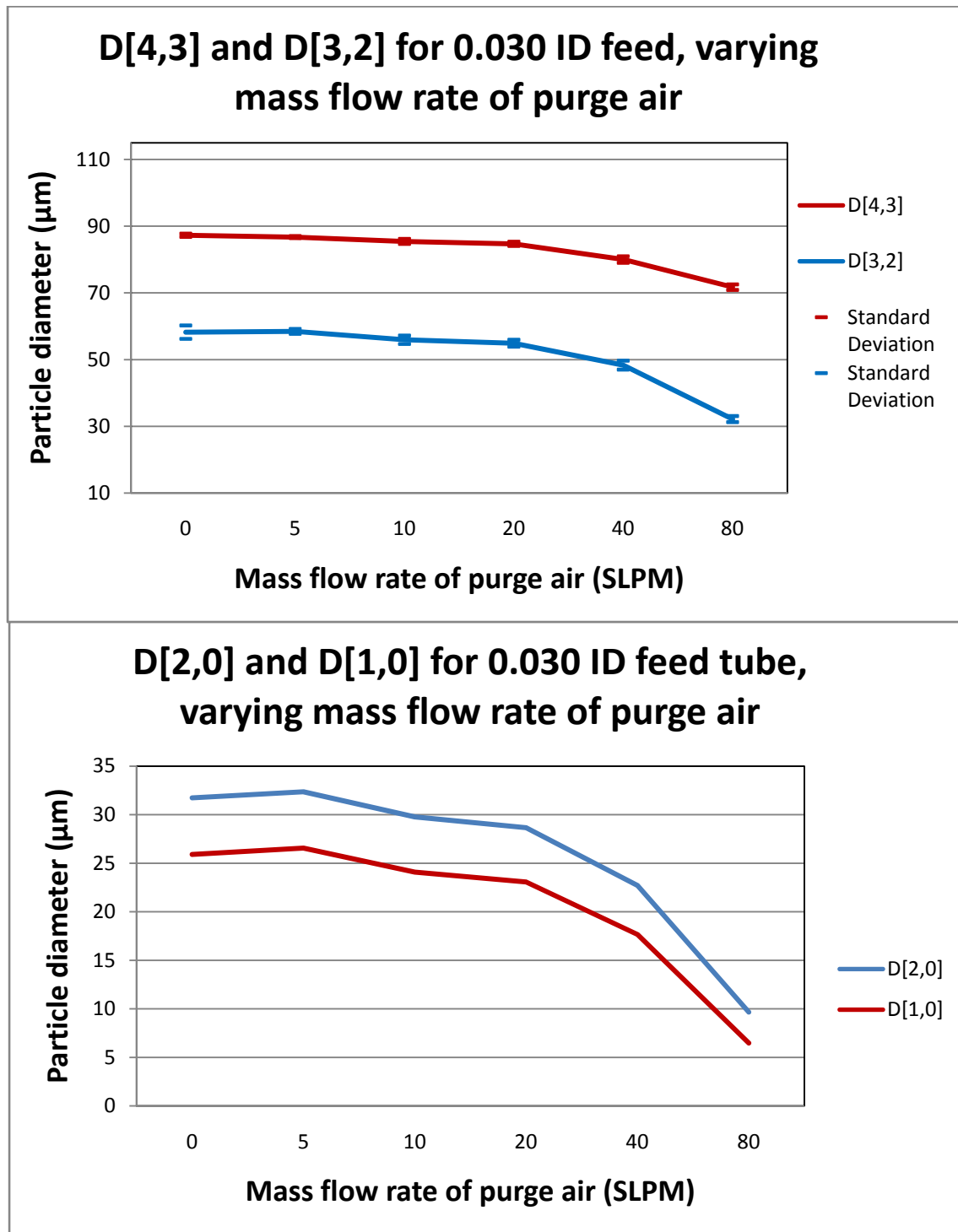


Figure 28: D[4,3], D[3,2], D[2,0] and D[1,0] for increasing mass flow rates of purge air co-flow, 0.030 inch ID feed, 0.25 inch ID shroud.

## 4.2 Labview Analysis

Analysis begins with computing isentropic values and properties for each project, to include Mach number, dynamic and kinematic viscosity, Reynolds number, and velocities before and after the shock wave using pressure and temperature averages from the Labview program and the equations from isentropic compressible flow theory. Table 3 summarizes the characteristics of projects 1, 2, and 7 below

**Table 3: Project 1, 2, and 7 theoretical flow properties and characteristics.**

Project	1	2	7 (6 x 6)
$P_o$ (Measured stilling chamber psia)	34.4	22.6	35.4
$P_1$ (Measured test section psia)	1.10	0.76	4.32
$T_o$ (Measured stilling chamber K)	299.0	292.2	266.7
$T_1$ (Temp before shock K)	111.9	111.1	146.4
$T_2$ (Temp after shock K)	138.0	136.6	NA
$M_\infty$ (Mach number free stream)	2.89	2.86	2.023
$V_\infty$ (Velocity free stream m/s)	613.1	603.2	491.7
$V_y$ (V-component after shock m/s)	98.8	97.1	NA
$\rho$ (Density kg/m <sup>3</sup> )	0.2369	0.1653	0.7102
$\mu$ (Dynamic viscosity PA·s)	$7.718 \times 10^{-6}$	$7.658 \times 10^{-6}$	$7.128 \times 10^{-6}$
$\nu$ (Kinematic viscosity m <sup>2</sup> /s)	$3.258 \times 10^{-5}$	$4.632 \times 10^{-5}$	$1.00 \times 10^{-5}$
$l$ (Representative length m)	0.4262	0.4262	1.0
Re (Reynolds number)	$8.02 \times 10^6$	$5.55 \times 10^6$	$3.38 \times 10^7$



Notable differences in the densities and Reynolds numbers are due to the different control pressures for projects 1, 2 and 7. Project 7 in the 6 x 6 inch tunnel has a decrease in Mach number and free stream velocity, but higher density and Reynolds number than the projects in the 2.5 x 2.5 inch tunnel. Projects 3-6, all similar because of the identical control pressure settings, are shown in Table 4 summarizes the isentropic properties for these projects.

**Table 4: Project 3-6 theoretical flow properties and characteristics.**

	Project 3	Project 4	Project 5	Project 6
$P_o$ (psia)	24.7	24.8	24.8	24.8
$P_1$ (psia)	0.878	0.895	0.893	0.890
$T_o$ (K)	288.8	286.9	286.9	287.4
$T_1$ (K)	111.3	111.1	111.0	111.1
$T_2$ (K)	136.6	136.3	136.2	136.3
$M_\infty$	2.82	2.81	2.81	2.82
$V_\infty$ (m/s)	597.1	594.3	594.4	595.1
$V_y$ (m/s)	96.0	95.5	95.5	95.7
$\rho$ (kg/m <sup>3</sup> )	0.1896	0.1936	0.1933	0.1925
$\mu$ (PA·s)	$7.675 \times 10^{-6}$	$7.659 \times 10^{-6}$	$7.654 \times 10^{-6}$	$7.661 \times 10^{-6}$
$\nu$ (m <sup>2</sup> /s)	$4.049 \times 10^{-5}$	$3.957 \times 10^{-5}$	$3.959 \times 10^{-5}$	$3.980 \times 10^{-5}$
$l$ (m)	0.4262	0.4262	0.4262	0.4262
Re	$6.29 \times 10^6$	$6.40 \times 10^6$	$6.40 \times 10^6$	$6.37 \times 10^6$

### 4.3 PIV Analysis

The recipe for PIV analysis begins with applying a mask over the ramp to projects one and two decrease computation time and to disregard any false signals generated by the ramp. Next, an adaptive correlation with a 75% overlap produces an initial velocity vector map for each image pair. The 75% overlap, vice 25% or 50%, increases the number of velocity vectors, and hence the fidelity of the test section velocity vector map. Following the adaptive correlation, a range validation removes any vectors grossly different from the velocities predicted by isentropic flow theory. The range gates for this range validation are 100 m/s to 900 m/s for the x-component of velocity (U), -150 m/s to 150 m/s for the y-component of velocity (V), and 100 m/s to 1000 m/s for the total velocity. Only valid velocity vectors continue to the next step, not moving averages or neighborhood validations that unnecessarily smooth the data in close proximity to the shock wave. The final step is a summing and averaging of the vector maps providing a single velocity vector map, or vector statistics, of the flow field. This final vector map provides the means to further analyze the data by producing scalar plots of U and V for the entire image, profile plots of V through the shock in order to characterize relaxation time and profile plots of U in order to characterize the boundary layer.

Due to the incorrect pulse delay and inability to correct for it in the Dantec Dynamic Studio software, scalar plots with velocity vectors are from TecPlot360 with a correction of the velocities. Boundary layer and relaxation time curve fits and calculations are from an import of data into Matlab following a correction of velocities in Excel.

Three major components of the flow are notable in the initial analysis of the scalar plots from the vector statistics data. First, the free stream velocity provides an easy check of the PIV system and tunnel as a whole in regards to isentropic flow theory accuracy. Secondly, the boundary layer provides another means of checking the fluid following characteristics of the CO<sub>2</sub>. Finally, plotting V throughout the vector field shows the ability of the CO<sub>2</sub> to correctly display and model the shock and expansion waves from the ramp in the test section.

Initial inspection provides a look at the accuracy of the free stream velocity PIV calculations. Figure 29 shows the scalar plots of U with vector overlays for projects 1 and 2.

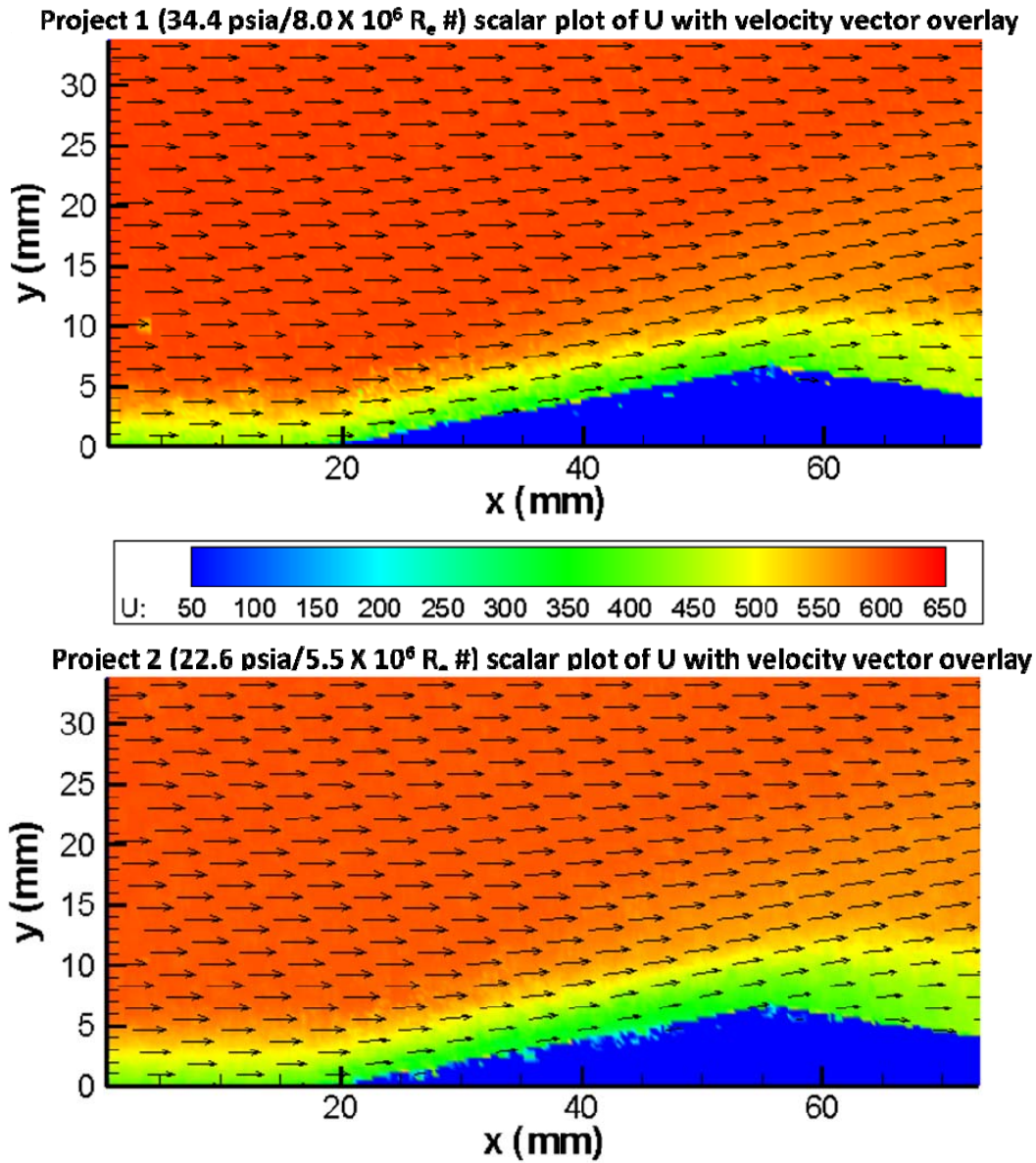


**Figure 29: Scalar plots of U with velocity vector overlay for projects 1 and 2.**

The free stream velocity prior to the ramp appears correctly according to scale and the boundary layer is clearly shown. Further analysis of the free stream velocity by plotting the velocity normalized according to Table 3 isentropic free stream velocities confirms the accuracy of the PIV system in tracking the fluid flow prior to the ramp in Figure 30.

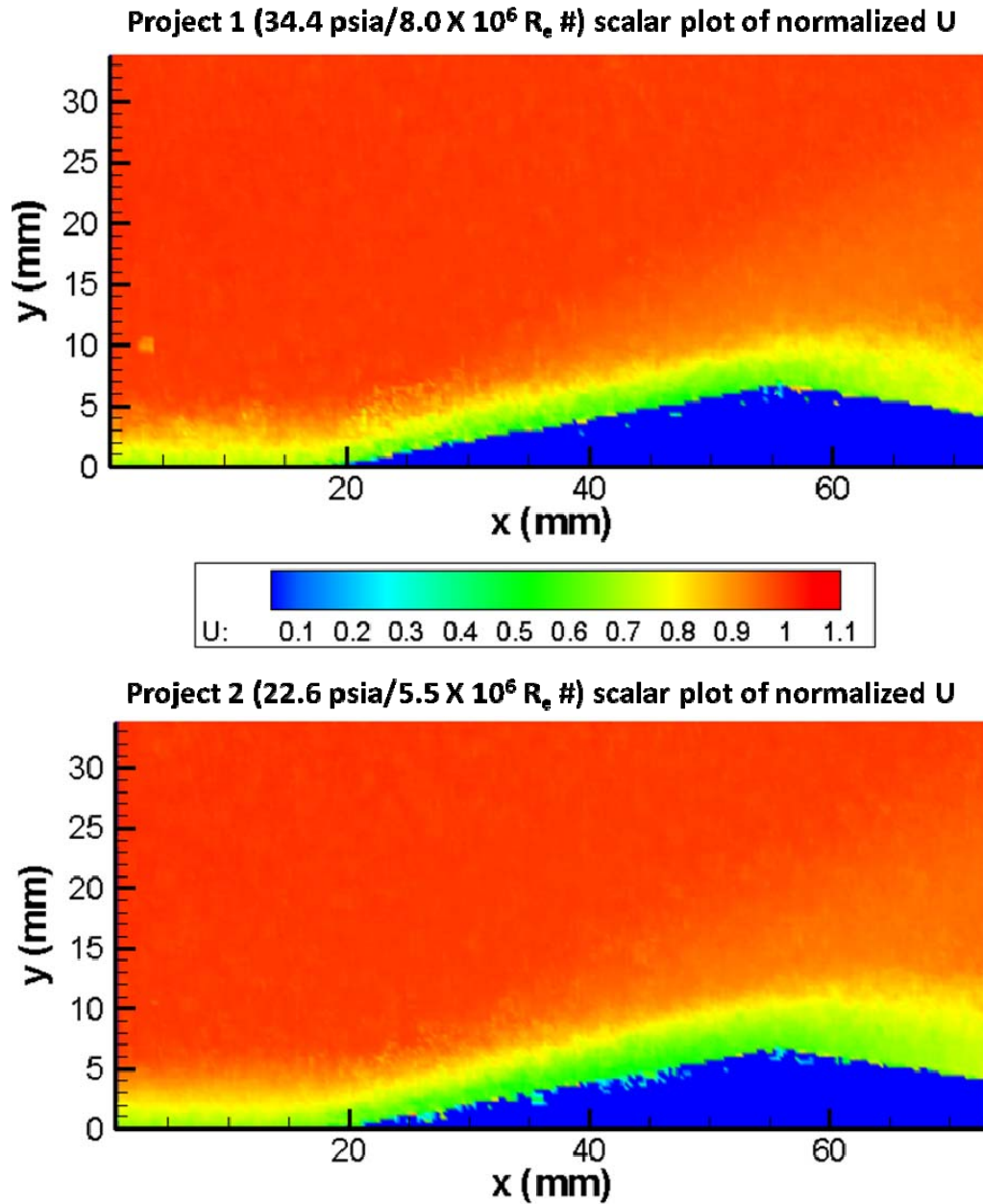


**Figure 30: Normalized U scalar plot for projects 1 and 2 ( $U_{\infty} = 613.1$  m/s for project 1, 603.2 m/s for project 2).**

Notice that qualitatively the boundary layer (99% of free stream velocity corresponding to 0.99 on the scale) appears larger in project 2 than it does in project 1 in Figure 3. This

correctly models the trend of compressible turbulent boundary layer theory in equation (22) of decreasing boundary layer height with increasing Reynolds number.

Project seven provides unique challenges in that the mass flow rate of air for the 6 x 6 tunnel is far greater than the 2.5 x 2.5 tunnel, providing a less dense seeding. Also, the differences in sublimation effects caused by the longer distance from settling chamber to the nozzle complicate the attempt at scale up. The same injector system provides the following typical images from project seven showing a decrease in seeding density

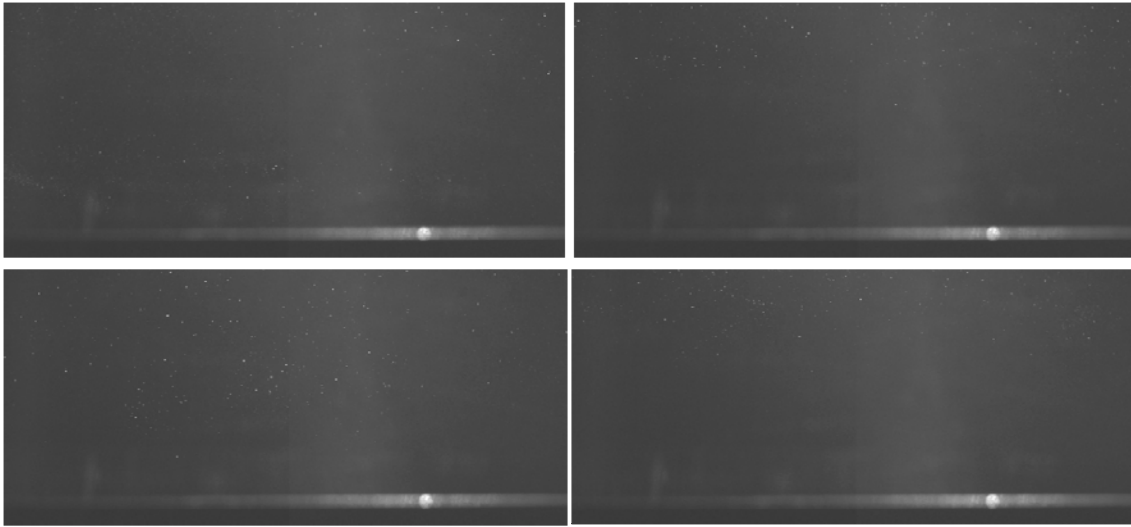


**Figure 31: Typical images from project 7.**

Notice the seeding population difference in comparison with the typical images in Figure 21 for the 2.5 x 2.5 inch tunnel. The runs in the 6 x 6 tunnel also show a decreasing seeding density as the run progresses, showing the effects of the air mass flow rate overpowering the CO<sub>2</sub> mass flow rate. In addition, the first image in Figure 31 is one of the few image pairs with particles resident in the boundary layer. The U scalar plot with velocity vector overlay in Figure 32 portrays the lack of useful data, particularly in the

boundary layer, due to the decrease in mass flow ratio of CO<sub>2</sub> to air despite 199 image pairs

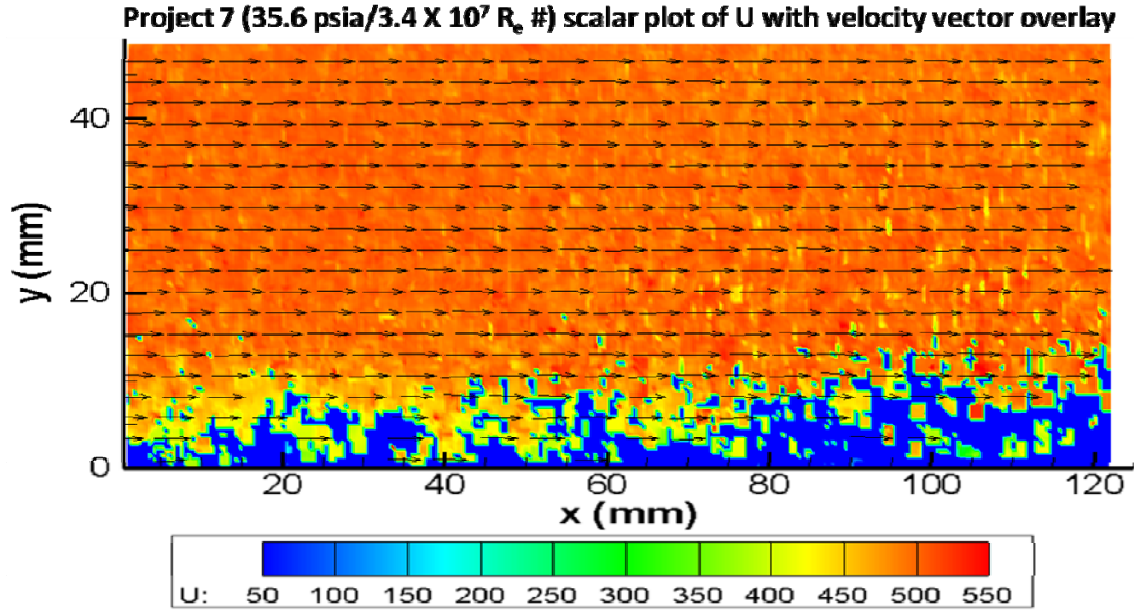


**Figure 32: Scalar plot of U with velocity vector overlay for the 6 x 6 tunnel.**

The majority of holes in the data occur in the boundary layer, allowing for a good free stream velocity comparison as shown in the normalized U plot in Figure 33 below

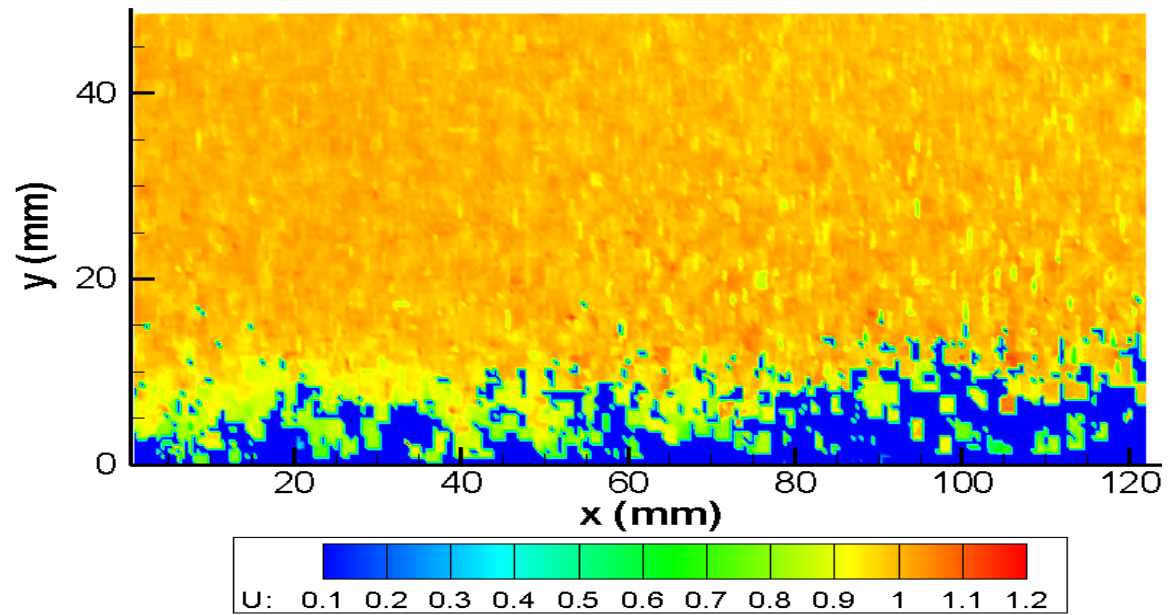
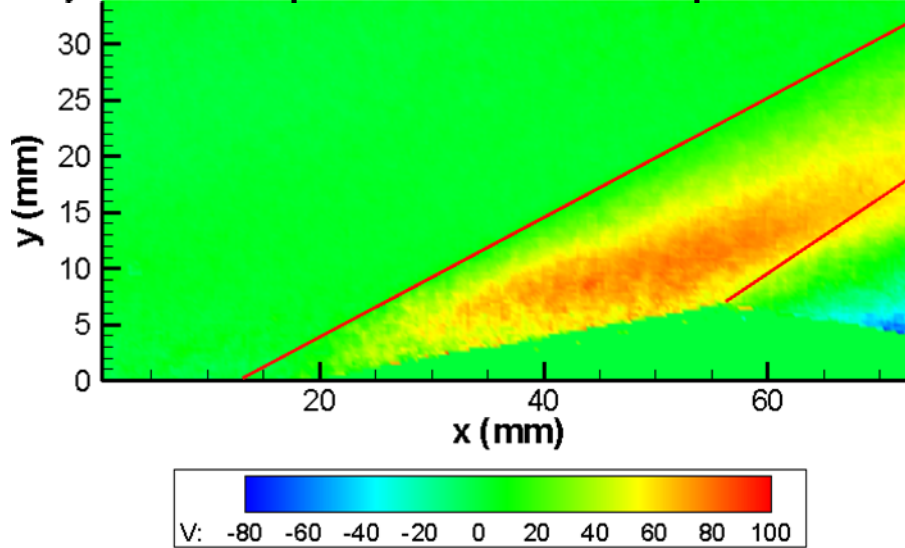


**Figure 33: Scalar plot of normalized  $U$  for the 6 x 6 tunnel ( $U_\infty = 491.7 \text{ m/s}$ ).**

The last initial analysis characteristic of the flow for project one and two is the modeling of the shock and expansion waves, clearly visible in a scalar plot of  $V$  in Figure 34 below



**Project 1 scalar plot of V with shock/expansion overlay**



**Project 2 scalar plot of V with shock/expansion overlay**

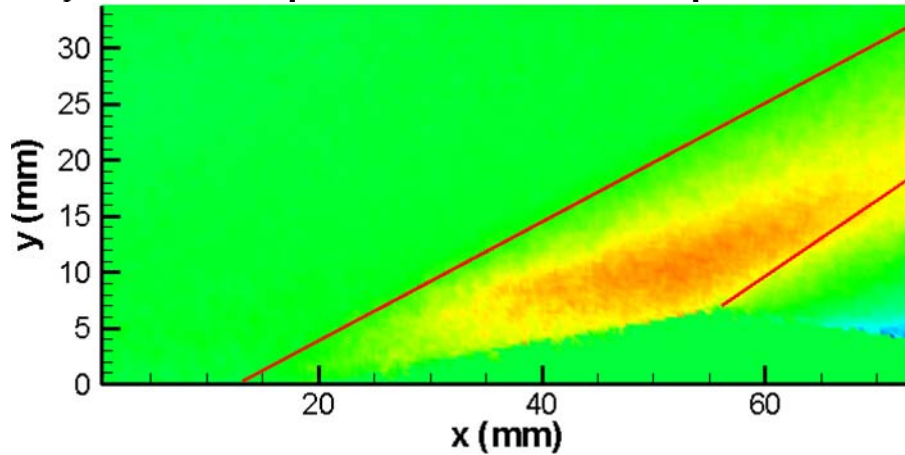


**Figure 34: Scalar plots of V for projects 1 and 2 with a display of theoretical shock and expansion wave locations.**

A shift is noticeable when comparing the location of the first noticeable change in V with the overlay of theoretical shock (28.5 degrees) and expansion (38.4 degrees) angles, demonstrating the effects of the particle lag response.

With confirmation of the PIV accurately capturing the flow characteristics, further analysis continues with an analysis of profile plots. Profile plots from the five different locations shown in Figure 36 for projects one and two provide a method for quantitatively analyzing the free stream and boundary layer, and provide a method for analyzing relaxation time for the CO<sub>2</sub> particles.

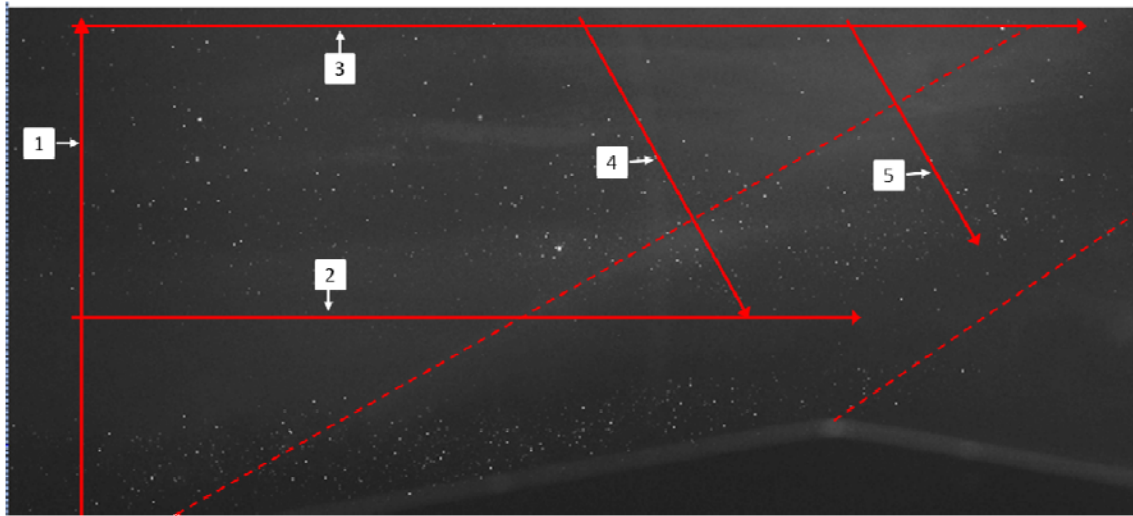


**Figure 35: Profile plot locations with visual shock wave location and theoretical expansion wave location.**

The first profile provides quantitative data to characterize the boundary layers for each project. By exporting U along this profile to Excel and applying the correction to velocities, a boundary layer analysis provides quantitative data to confirm the ability of the CO<sub>2</sub> to follow the flow in the boundary layer. Exporting the data from Excel to Matlab, allows the use of the curve fitting tool in Matlab to perform a non-linear curve fit with equation (23). The graphs in Figure 36 show the results of the non-linear curve fits of equation (23) from Matlab for projects one and two, profile one in comparison to the experimental data.

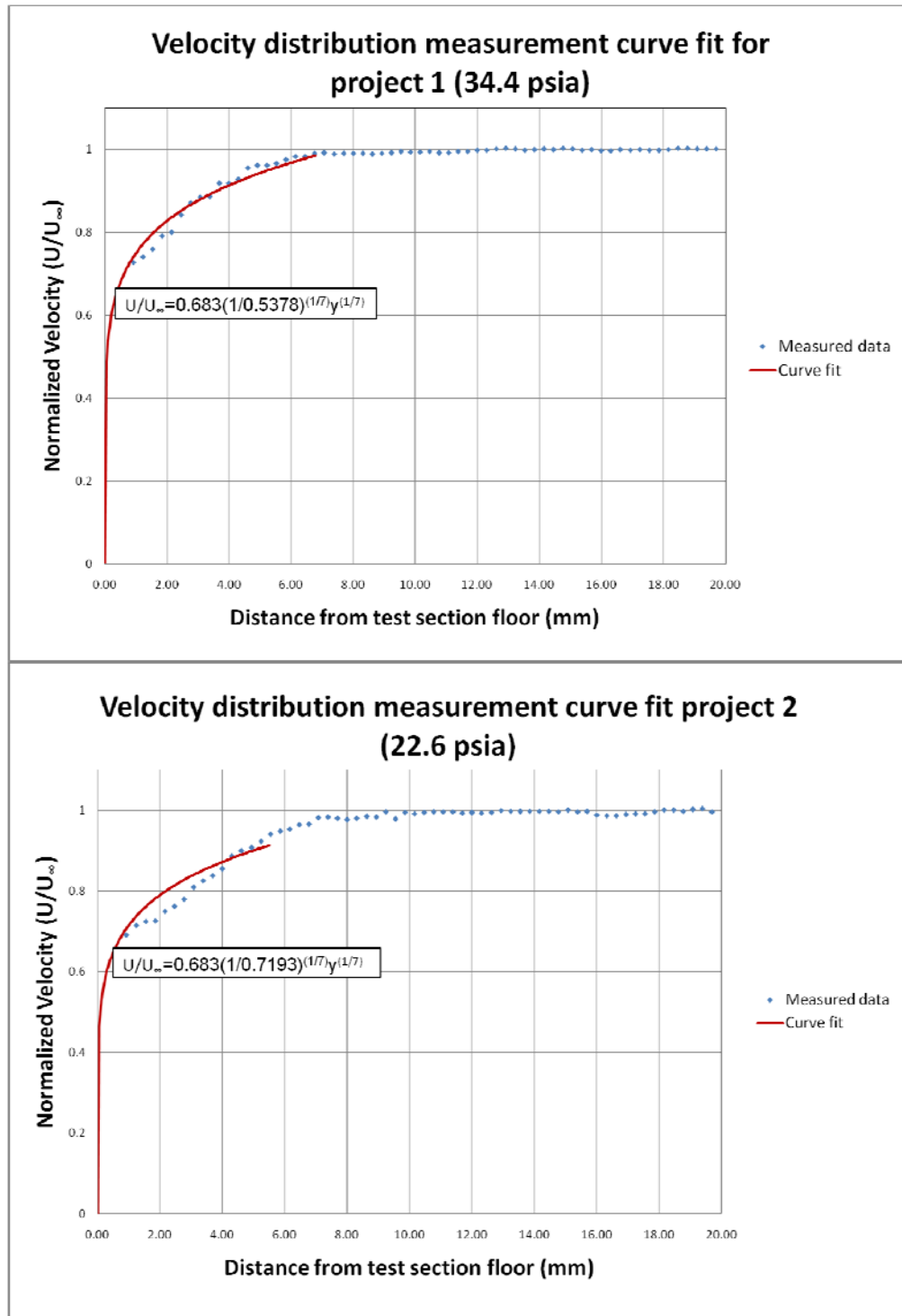


**Figure 36: Curve fits for boundary layers in projects 1 and 2 ( $U_\infty = 613.1$  and  $603.2$  m/s respectively) with curve fit equation showing value for  $\delta_2$ .**

Similar profile plots from project seven produces unsatisfactory results due to lack of data as the highest  $R^2$  value obtainable is 0.2903. In order to characterize the boundary layer, the average velocity for the data for every profile plot across the width of the image are input into the curve fit. The average profile plot does not characterize the boundary layer in one particular location as in projects one and two, but does provide a means to analyze and characterize an average boundary layer throughout the image minus the locations lacking data. These locations are easily distinguishable by the value of velocity equaling zero. The results of this curve fit with equation (23) are shown in Figure 37 below.

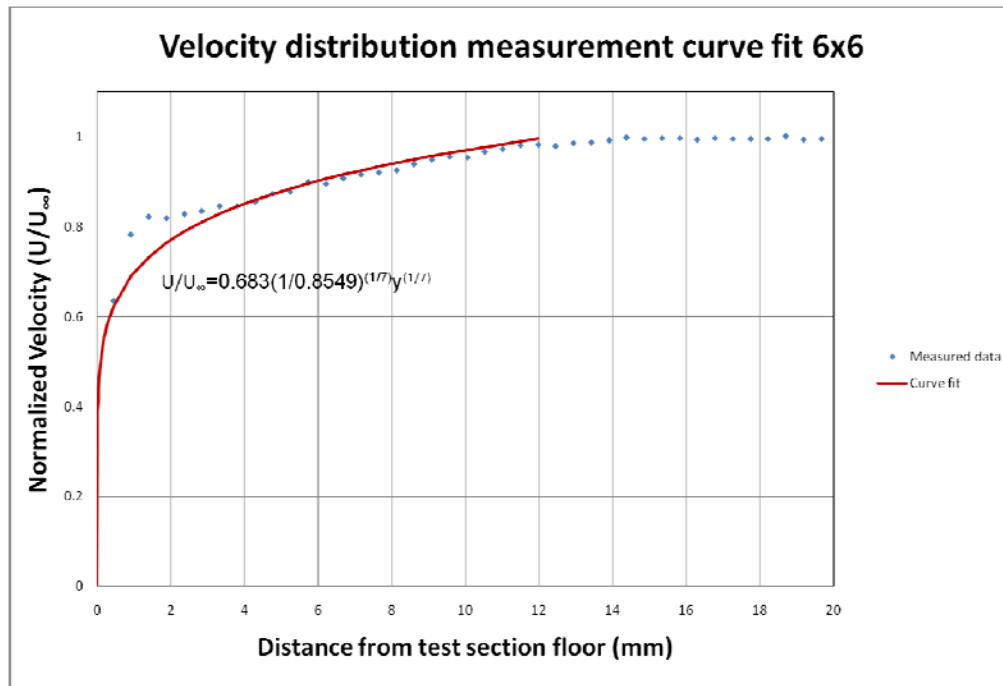


**Figure 37: Curve fit for boundary layer in project 7 ( $U_{\infty} = 491.7$  m/s) with curve fit equation showing value for  $\delta_2$ .**

Figures 36, 37 and 38 also contain quantitative free stream velocity comparisons between isentropic theory from Table 3 and the experimental data points, shown as the scatter of data points about the y-axis value of 1.0 beyond the boundary layer. For reports one and two the normalized velocity averages and standard deviations for profile plot 1 above 1500 pixels or 14.8 mm are shown below, and for project seven the normalized average is taken from the compressed boundary layer plot data above 20 mm and displayed below.

**Table 5: Normalized velocity average and standard deviation for projects 1, 2 and 7.**

	Average ( $U/U_\infty$ )	Standard Deviation ( $U/U_\infty$ )
Project 1 ( $U_\infty = 613.1$ m/s)	0.9970	0.00404
Project 2 ( $U_\infty = 603$ m/s)	0.9967	0.00482
Project 7 ( $U_\infty = 492$ m/s)	0.9986	0.00241

Additional curve fits with equation (24) using the same procedure described above, theoretical calculations from equation (22) and the first occurrence of experimental values equaling  $0.99 \cdot U_\infty$  along the plots all compare favorably in determining values for  $\delta$  in Table 6 below.

**Table 6: Boundary layer comparisons for projects 1 and 2.**

	Experimental (1 <sup>st</sup> occurrence of $0.99*U_{\infty}$ ( $\delta$ in mm))	Theory (Eq. 22) ( $\delta$ in mm)	Curve fit (Eq. 23) ( $\delta$ in mm)	Curve fit (Eq. 24) ( $\delta$ in mm)
Project 1	6.77	6.56	5.53 $R^2 = 0.959$	6.42 $R^2 = 0.956$
Project 2	8.62	7.06	7.40 $R^2 = 0.919$	8.73 $R^2 = 0.889$
Project 7	11.50	10.7	10.15 $R^2 = 0.939$	8.79 $R^2 = 0.900$

Quantitatively, project one and two follow theory by showing an increase in boundary layer height at the same location for an increase in Reynolds number of the flow.

The remaining four profile plots in Figure 31 are taken from projects one through seven and provide the data to characterize the relaxation time. Profile two and three plot  $V$  along a horizontal profile with profile three being higher in the test section, while profile four and five are profiles normal to the shock wave as in et al. (2003). Profile four extracts  $V$ , while profile 5 mimics Scarano et al. (2003) by converting  $U$  and  $V$  into the normal to the shock component of velocity. Figure 38 portrays the theoretical graph for project two, profile five, of multiple particle diameters normal velocity relaxation response across a shock wave.

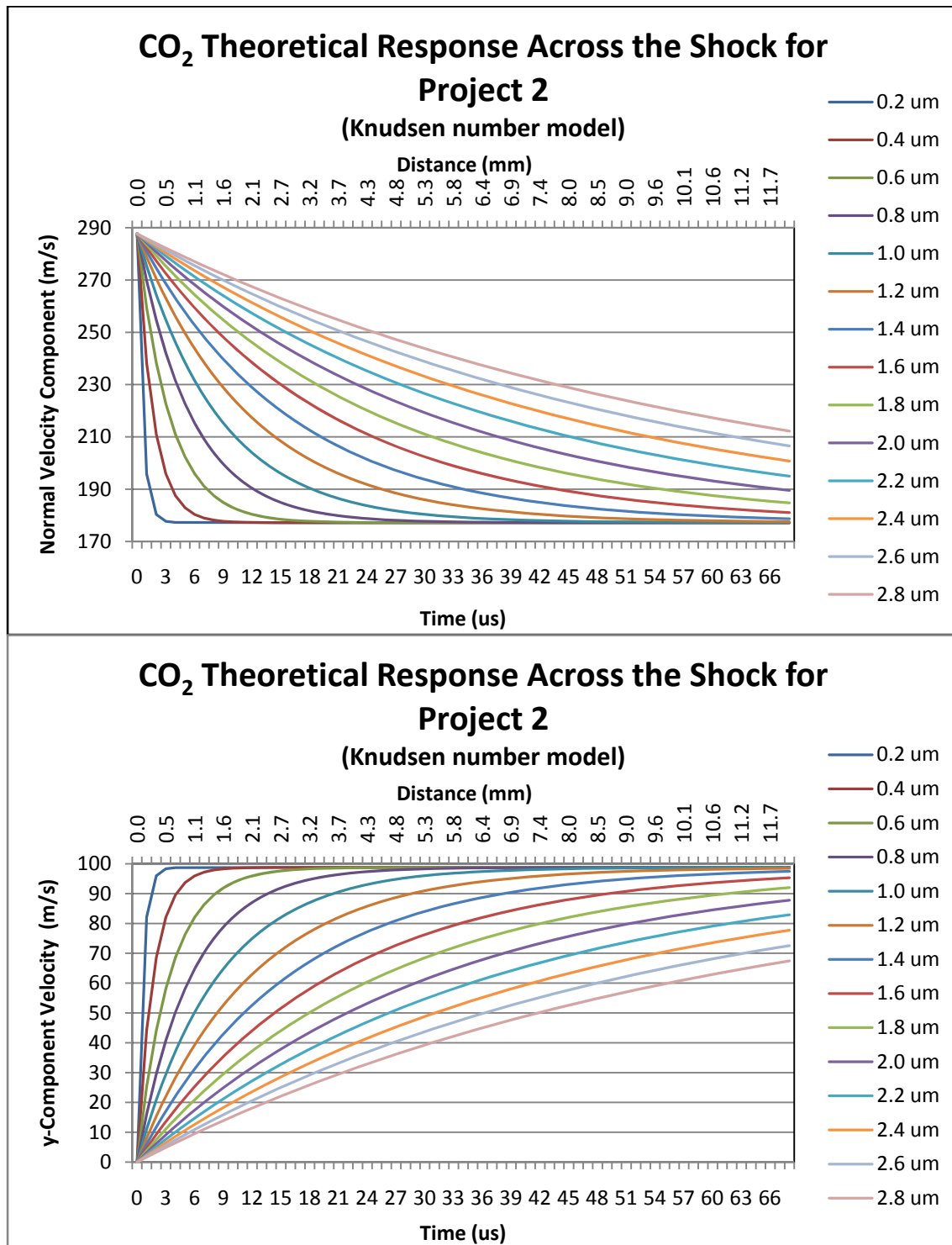


**Figure 38: Normal and y-component of velocity theoretical relaxation response of multiple particle diameters for project 2.**

The distance beyond the shock for profiles two and three is 20 mm while profile four has a distance of 6 mm and profile five a distance of 10 mm corresponding to times of approximately 30  $\mu$ s time beyond the shock except profile five which has a time of 42  $\mu$ s. Just by looking at the velocities at the end of each profile, a rough estimate of the particle response time by comparison to the theoretical models in Figure 38 is achievable. Another export of the data to Excel in order to correct velocities precedes another nonlinear curve fit in Matlab to yield relaxation times according to equation (15). Figure 39 shows the curve fit models versus the experimental data for projects one and two, profile five, as this profile most closely resembles the work of Scarano et al. (2003)



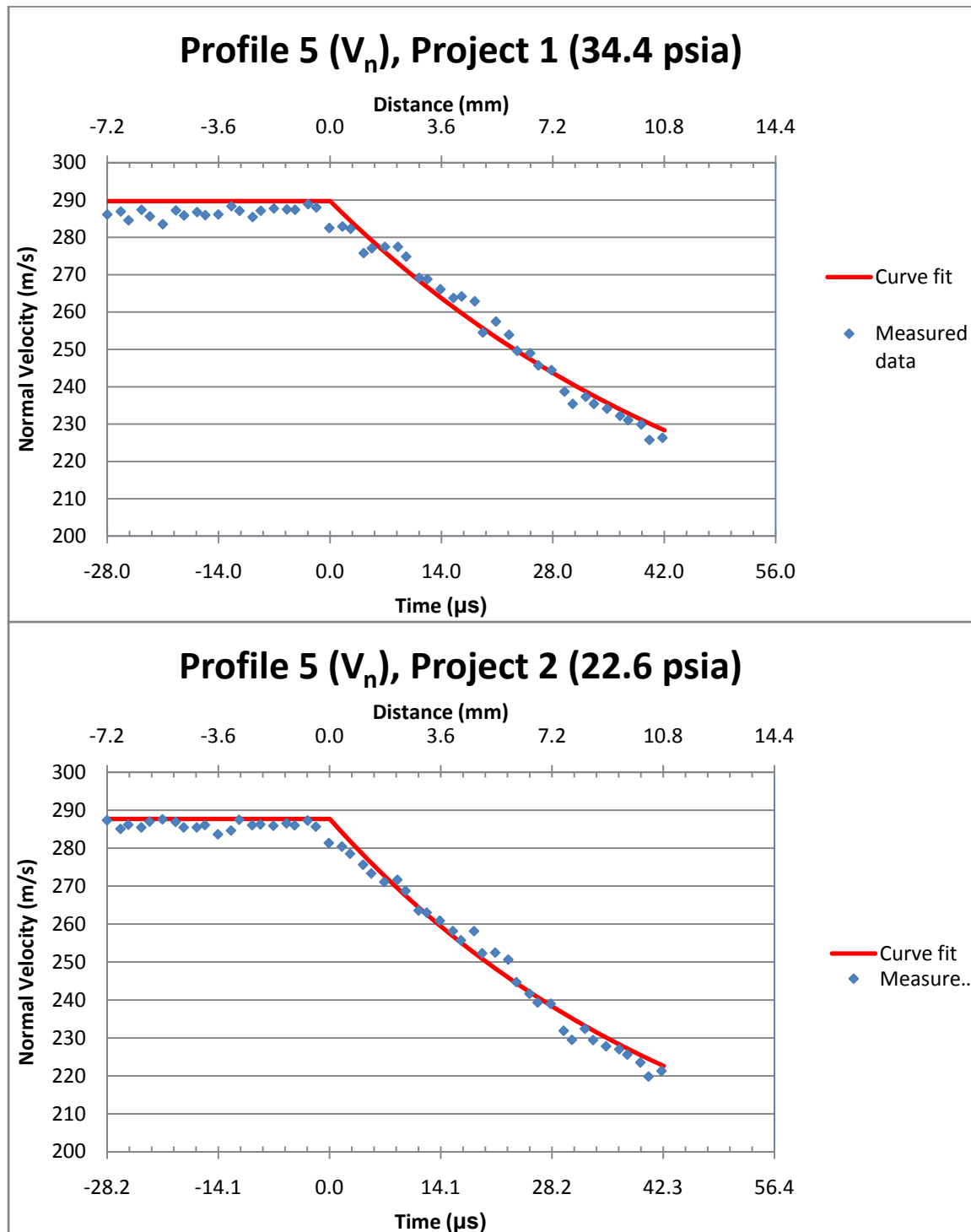


**Figure 39: Curve fits of relaxation time for profile 5 ( $V_n$ ), project 1 (34.4 psia) and 2 (22.6 psia) versus distance (mm) and time ( $\mu$ s).**

Relaxation times for the curve fits of experimental data with equation (15) for each project and profile are shown in Table 7 below

**Table 7: Particle relaxation times and diameters for projects 1-6, profiles 2-5.**

	$\tau_p$ ( $\mu$ s) Profile 2	$\tau_p$ ( $\mu$ s) Profile 3	$\tau_p$ ( $\mu$ s) Profile 4	$\tau_p$ ( $\mu$ s) Profile 5
Project 1	25.1 $R^2 = 0.986$	38.9 $R^2 = 0.950$	42.46 $R^2 = 0.937$	52.99 $R^2 = 0.971$
Project 2	25.5 $R^2 = 0.933$	37.33 $R^2 = 0.781$	39.02 $R^2 = 0.939$	47.57 $R^2 = 0.978$
Project 3	27.77 $R^2 = 0.8917$	43.27 $R^2 = 0.890$	25.06 $R^2 = 0.834$	45.68 $R^2 = 0.964$
Project 4	27.06 $R^2 = 0.700$	35.26 $R^2 = 0.4613$	37.54 $R^2 = 0.903$	44.09 $R^2 = 0.835$
Project 5	29.54 $R^2 = 0.826$	36.93 $R^2 = 0.695$	50.79 $R^2 = 0.783$	45.50 $R^2 = 0.969$
Project 6	18.04 $R^2 = 0.654$	41.48 $R^2 = 0.601$	35.88 $R^2 = 0.699$	48.40 $R^2 = 0.934$

Profiles two (lower horizontal profile with V) and four (lower normal profile with V) seem to provide results that indicate a smaller relaxation time and particle diameter, but these profiles take data in close proximity to the boundary layer as the flow progresses over the ramp. Profile three (higher horizontal profile with V) seems to indicate smaller

relaxation times and particle diameters as well, but since profile five is the model most closely resembling the model of Scarano et al. (2003), and additionally provides the most consistent and best fit data according to  $R^2$  values, its data provides the basis for particle diameter calculations. The particle diameters, simple and Knudsen model, from equations (13) and (14) are shown in Table 8 for the density range of  $1180 \text{ kg/m}^3$  to  $1800 \text{ kg/m}^3$  for  $\text{CO}_2$ .

**Table 8: Particle diameters for profile 5, simple and Knudsen model.**

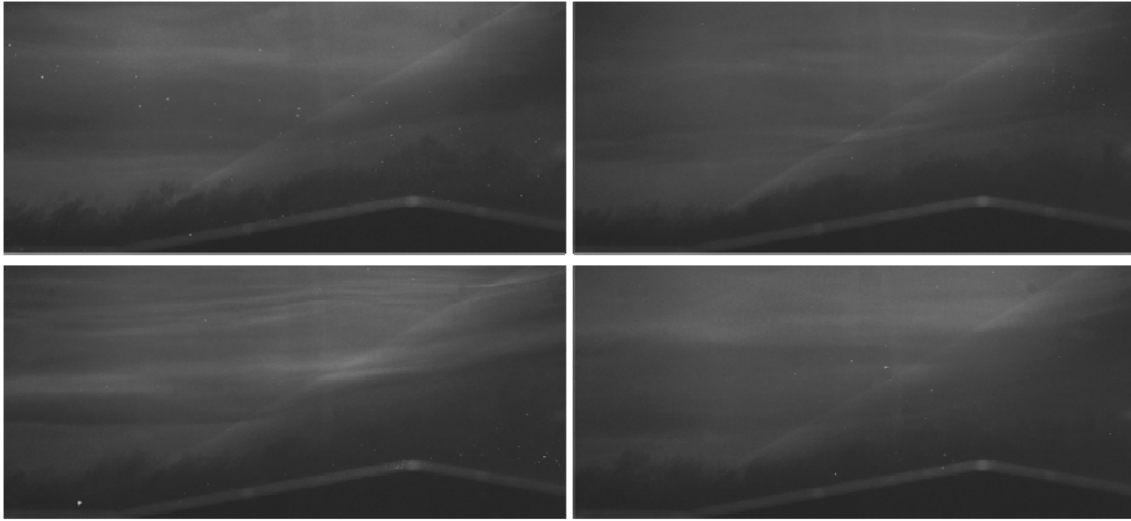
	Particle diameter ( $\mu\text{m}$ ) Simple model	Particle diameter ( $\mu\text{m}$ ) Knudsen model
Project 1	2.02-2.50	1.93-2.40
Project 2	1.91-2.36	1.81-2.26
Project 3	1.87-2.31	1.78-2.22
Project 4	1.84-2.27	1.74-2.17
Project 5	1.87-2.30	1.77-2.21
Project 6	1.93-2.38	1.83-2.28

Project 1 and 2 demonstrate more image pairs provide better fits of the data (higher  $R^2$  values) and provide very similar results. Also notice that projects two and three provide consistent results as both are at the same control pressure with only a slight difference in

injector (one with T-junction, one without). Although Kochtubajda et al. (1985:604) states temperature has the biggest impact on CO<sub>2</sub> sublimation rate, higher pressures also reduce the sublimation rate (Kochtubajda et al., 1985:599). Project one's higher control pressure (34.4 psia) would cause an increase in particle diameter due to a decrease in sublimation in comparison with project two (22.6 psia), thereby accounting for the increase in relaxation times and corresponding particle diameters in the test section.

Projects three through six do not demonstrate decreasing relaxation times and particle diameters as the Malvern sizing data for increasing amounts of co-flow purge air would lead one to believe. Although Table 6 does not support this claim quantitatively, the data does exhibit decreasing  $R^2$  values due to the decrease in seeding density in the test section. This decrease in seeding density is attributable to a decrease in particle size causing an increase in condensate, thereby decreasing the amount of particles suitable for PIV analysis. This increase in condensate is shown qualitatively in Figure 40 and confirms a particle size manipulation is occurring.

**Project 6 (80 SLPM purge)**



**Project 2 (no purge)**

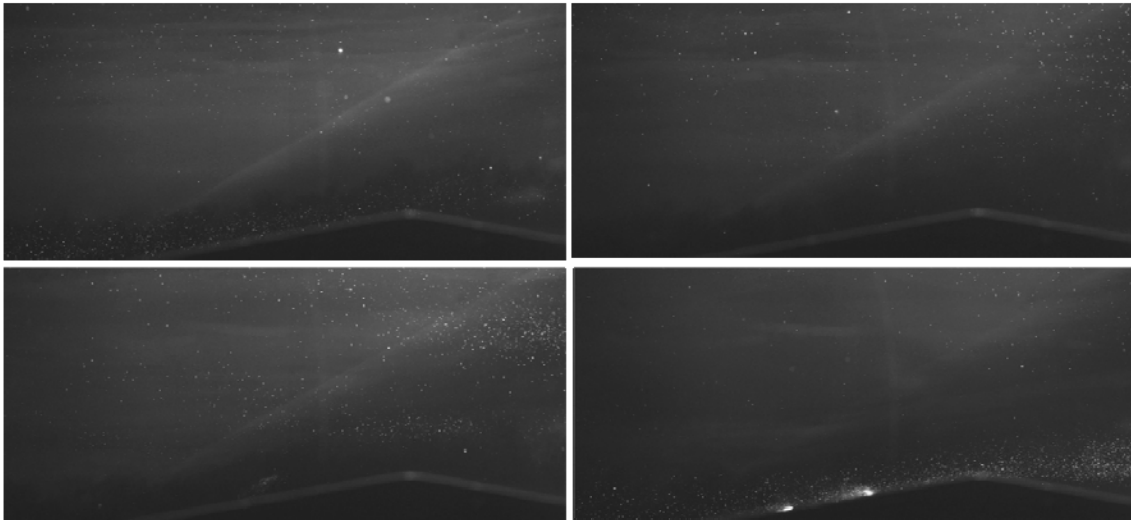


**Figure 40: Typical image from project 6 (80 SLPM) and project 4 (no purge).**

Further displaying this decrease in useful data, Figure 41 displays normalized  $U$  with an increase in the lack of data shown by the increase of regions with a value of 0.

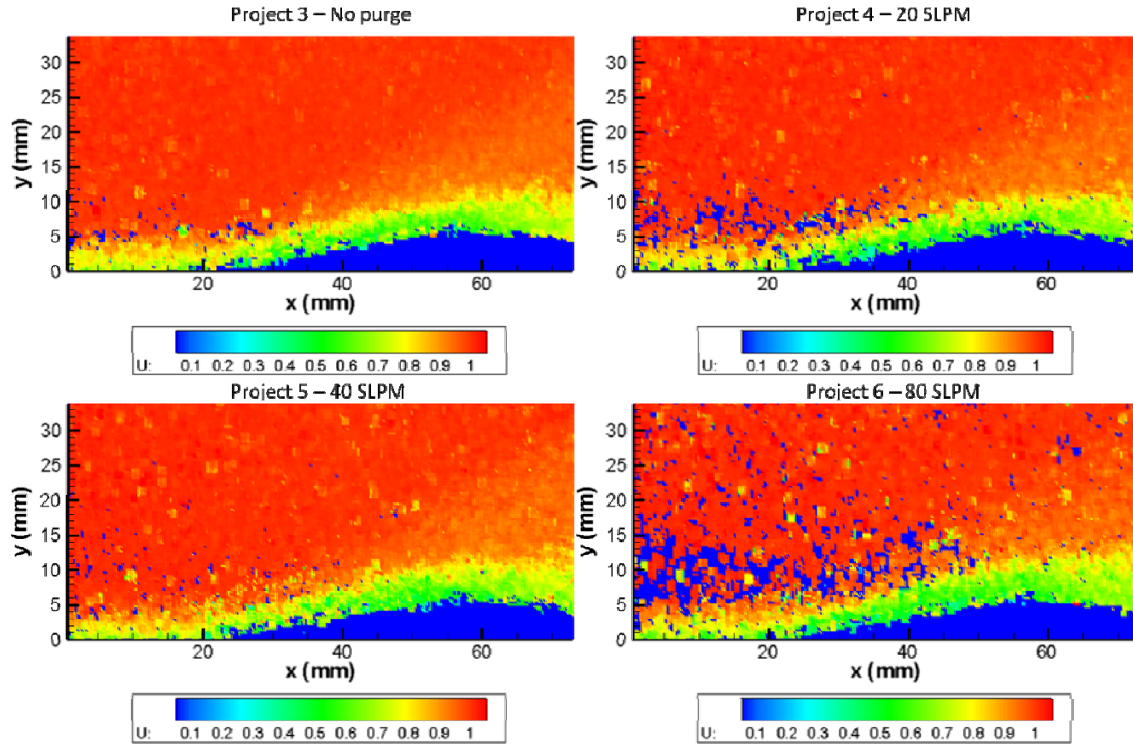


**Figure 41: Normalized U scalar plots for projects four through six ( $U_{\infty} = 597.1$ , 594.3, 594.4 and 595.1 m/s respectively).**

Qualitatively the particle size indicates a decrease with the addition of purge air. One possible explanation for the lack of quantitative confirmation is insufficient data collection. Another explanation is the data is correct due to a property of the  $\text{CO}_2$  particles. It is possible that any injected particles smaller than the particle size that survives to be on the order of two microns in the test section, sublime completely and then condense to produce the fog seen in the test section. In this case, the relaxation time characterization above would be the lowest achievable relaxation time using  $\text{CO}_2$  in the manner of this research.

#### 4.4 Sources of Error

A source of error for the Malvern particle sizing is human error in placing the injector so the plume of CO<sub>2</sub> is centered on the laser beam. Each time a different shroud or feed tube was replaced it involved taking the injector apart and attempting to realign the plume through the laser. As the purge air set-up did not require realigning the plume, these results are more consistent relative to each other due to the lack of disturbance of the plume placement. Also, the volume bias is shown in the Figures exhibiting contrasting trends in D[4,3] and D[3,2].

The biggest source of error in the PIV portion of the experiment is the incorrect pulse delay sent by the system. For the pulse setting in use, this corresponds to a 12.2% error in all velocities. Without the discovery of this error the results would display inaccuracy and would be suspect due to the results' divergence from theory.

PIV has limitations when applying it to relaxation time calculations. The first is spatial resolution, or the relatively large size of the interrogation window. Secondly, although increased from Peltier (2007), the temporal resolution has limits as well. Additionally, the shock location is not constant due to free stream turbulence or ensemble averaging (Scarano et al., 2003:435). Locating the shock using the visualization due to condensation shows the shock location moves by as much as 30 pixels, or 1.12 mm, definitely impacting the relaxation time calculation.

A further source of error is the compressing of data across the x axis range in the analysis of project seven's boundary layer. The method of averaging by including all valid values is not uniform across the x axis range, therefore the boundary layer analysis

does not provide an analysis of the average boundary layer. Although it averages the data, it does produce enough data points to allow for curve fit with an appropriate  $R^2$  value, unlike the attempts at random profile plot analysis.

Another source of error is the lack of image pair data acquisition in projects four through six, due to the decrease in seed particle density. This lack of acquisition does not provide enough data to establish a trend for relaxation time or particle diameter.

Two special notes are worthy of mention in order to assist future researchers. First, the  $\text{CO}_2$  must be pure and the injector clear. One bottle of  $\text{CO}_2$  was found to flow intermittently and clog the injectors. After extensive troubleshooting of the injector, which had been found to cause flow problems previously, no problems with the injector were discovered. It is assumed the  $\text{CO}_2$  in this bottle was somehow contaminated or impure causing the clogging of the injector. After replacing the bottle, the same injector provided a steady and uninterrupted flow. The second note is the computer running the PIV system experienced problems when running next to the 6 x 6 tunnel. The vibrations, either seismic or acoustic, were causing the computer to stop operating, resulting in the PIV system not operating during the operation of the 6 x 6 tunnel. To correct this problem, foam padding was used to insulate the computer against vibrations and the PIV system operated normally thereafter.



## **5. Conclusions and Recommendations**

### **5.1 Results Summary and Conclusion**

Particle sizing is critically important in the use of clean seeding in PIV. The Malvern sizing data provides useful relative sizing information for use in clean seeding PIV. An increase in the length of the 0.25 inch ID shroud tube from 3 inches to 10 inches increased the Sauter mean ( $D[3,2]$ ) from 35.9  $\mu\text{m}$  to 52.6  $\mu\text{m}$ , an increase of over 46%. Further, an increase in shroud ID from 0.125 inches to 0.25 inches increases the Sauter mean from 17.8  $\mu\text{m}$  to 55.2  $\mu\text{m}$ , a 210% increase. Clearly, the shroud ID and length are important factors in the size of the particle exiting the feed/shroud injector. An insulated shroud tube produced a Sauter mean of 59.6  $\mu\text{m}$ , an increase of 8% from the shroud tube without insulation, yielding another method of increasing particle size. Decreasing the feed tube ID provides yet another way of increasing particle size.

Clearly reversing any of the methods above will decrease particle size. Another way to reduce particle size is to add a co-flow of purge air to the shroud tube. Increasing the amount of purge air decreases the particle size even further. A Sauter mean diameter decrease from 58.2  $\mu\text{m}$  for the 0.030 inch ID feed tube with a 10 inch long 0.25 inch ID shroud with no purge air addition, to 32.2  $\mu\text{m}$  with the addition of 80 SLPM of purge air corresponds to a 45% decrease in particle diameter. This quantitative information was confirmed qualitatively with a comparison between images from the no purge and 80

SLPM purge projects. While not providing absolute sizing information for use when injecting into the stilling chamber of a wind tunnel, the results provide a way to change the particle diameter relative to the feed tube and shroud tube in current use in order to obtain quality PIV results.

The 0.030 inch ID feed tube in combination with the 10 inch long 0.375 inch ID shroud tube is an injector that provides particles of sufficient size to provide accurate PIV results when injecting into the stilling chamber of the 2.5 x 2.5 inch AFIT supersonic wind tunnel. Upon inspection of the image pairs, it is clear the CO<sub>2</sub> condensate provides an image of the shock wave and the lack of condensate provides an image of the boundary layer. The analysis, using an adaptive correlation with a 75% overlap, does not use averaging or neighborhood validation in order to preserve fidelity around the shock. The interrogation region of 32 x 32 pixels corresponds to a 1.2 x 1.2 mm distance in the test section. On the initial qualitative inspection of the processed data, the particles accurately track the free stream velocity, the boundary layer, and the shock and expansion waves created by the 10 degree ramp in the test section. Qualitatively the average free stream velocity along profile one has an error of 0.3% for project one and 0.33% for project two.

Two different curve fits for project one and two provide values for the momentum thickness,  $\delta_2$ , and the displacement thickness,  $\delta_1$ . These values, in turn, provide values for the momentum thickness,  $\delta$ . Theoretical values of 6.56 mm and 7.06 mm for projects one and two respectively show the boundary layer increases in size for a lower Reynolds number flow. The two curve fits for project one yield values of 5.53 mm and 6.42 mm respectively, while the values for project two are 7.40 mm and 8.73 mm

respectively. Quantitatively the results are within 24%, but as close as 5% to the theoretical value. As this is a measurement along one profile and turbulent boundary layers are difficult to model at best, the CO<sub>2</sub> particles appear to correctly tracking the flow of the boundary layer.

Particle characterization by modeling the relaxation time of the particle across the shock provides a means to infer a particle diameter in the test section. The relaxation times for projects one and two when calculated according to the method outlined in Scarano et al. (2003) are 53.0 and 47.6  $\mu\text{s}$  respectively. Although this is well above the relaxation time of 2.4  $\mu\text{s}$  for the 0.2  $\mu\text{m}$  TiO<sub>2</sub> particles used by Scarano et al. (2003), the mean particle size in the test section inferred by these relaxation times is 1.8 to 2.4 microns depending on the density value used for CO<sub>2</sub>. These particle sizes are easily in the range of particle diameters (1-3  $\mu\text{m}$ ) of other commonly used seed materials in air such as DEHS, a glycol- water solution and vegetable oil (Tropea et al., 2007:288) While a trend in establishing differing relaxation times, and therefore varying test section particle sizes, due to the addition of increasing amounts of purge air was not established, a qualitative assessment leads to the inference of increased data collection and research yielding a trend.

This research provides the first attempt at scale up by attempting clean seeding PIV in the 6 x 6 inch AFIT wind tunnel using the same injector as the 2.5 x 2.5 inch wind tunnel. This injector provides suitable particles for PIV results. The decrease in seeding density due to an increase in the air mass flow rate is evident by examining the image pairs and the lack of condensate is also notable. The same recipe above was used to

analyze the data but it is apparent that decreased seeding density requires more data than the 199 image pairs have provided. Holes in the data forced a compromise to model the boundary layer. The average of  $U$  across the width of the field of view provided one average profile plot that produced satisfactory results when modeling the boundary layer. The curve fit values of 10.15 mm and 8.79 mm for the boundary layer thickness compared favorably with the theoretical value of 10.7 mm. The average free stream velocity, also calculated from the compressed profile plot, is within 0.14% of the isentropic theoretical free stream velocity.

## **5.2 Desired Impact of this Research**

The results of this paper provide another basic step for the utilization of clean seeding PIV in other applications. The ability to utilize the stilling chamber as a clean seeding injection location is extremely useful in order to minimize the disturbance of the fluid flow potentially caused by the  $\text{CO}_2$  injection. The relative particle sizing data will enable follow on researcher to continue using this location by adjusting particle size in order to produce particles suitable for PIV. By evaluating the image pairs, the PIV operator will be able to determine whether the particle size needs to be increased or decreased to produce optimum results and this paper provides the basic framework and various methods to accomplish this particle manipulation. The characterization of the

relaxation time helps to establish CO<sub>2</sub> as a viable and attractive alternative to other seeding materials.

### **5.3 Recommendations for Future Experimentation**

Future experiments should continue to focus on improving the injection device to make it more flexible and accurate. Possible improvements would be to incorporate a needle valve to eliminate the need to change feed tubes and to increase flexibility, the addition of a control valve to control the mass flow rate of CO<sub>2</sub> more accurately, and investigating the design of a multi-port injector to increase the mass flow rate of CO<sub>2</sub> thereby increasing seeding density.

Further research should also focus on investigating the effects of changing injector devices and particle size at the injection site. Decreases in relaxation time would confirm the ability to optimize the particle size by adjusting the injector to minimize relaxation time. Further research in the 2.5 x 2.5 inch AFIT wind tunnel should replace the Mach 3 nozzle with the Mach 1.9 nozzle in order to slow the velocities and obtain more data points in the relaxation distance. Additionally, the ramp could be made to extend a further distance in order to increase the distance between the shock wave and expansion wave. The longer ramp would necessitate a movement of the camera to encompass more of the shock and less of the boundary layer around the ramp.

## References

- Adrian, R. (2005). Twenty years of particle image velocimetry. *Experiments in Fluids*. Published online, Springer-Verlag.
- Allen, T. (1990). *Particle size measurement*. New York: Chapman and Hall.
- Anderson, J. (2003). *Modern compressible flow: with historical perspective*. Boston: McGraw Hill.
- Dantec Dynamics A/S (2002). *FlowManager software and introduction to PIV instrumentation: software users guide*. Publication No. 9040U3625. Dantec Dynamics, Skovlunde Denmark.
- DeLapp, C. (2006). *Particle image velocimetry using novel non-intrusive particle seeding*. MS thesis, AFIT/GAE/ENY/06-J01. Graduate School of Engineering and Management, Air Force Institute of Technology, Wright-Patterson AFB OH.
- Dowdell, R. (1974). *Flow: Its measurement and control in science and industry*. Instrument Society of America.
- Miles, R., Lempert, W., Forkey, J., Finkelstein, N., Harris, S. (1997). Optical Diagnostics for flows with density variations. (Fulachier, L., Lumley, J., Anselmet, F., eds). *Fluid Mechanics and its applications*. Dordrecht, Netherlands: Kluwer Academic Publishers.
- Kochtubajda, B. and Lozowski, E. P. (1985). The sublimation of dry ice pellets used for cloud seeding. *Journal of Climate and Applied Meteorology*, 24(6), 597-605.
- Kompenhans, Jürgen. (2006) Program for 12<sup>th</sup> International Symposium on Flow Visualization.  
[http://www.isfv.org/fileadmin/user\\_upload/Programme/ISFV12\\_program.pdf](http://www.isfv.org/fileadmin/user_upload/Programme/ISFV12_program.pdf)
- McNiel, C. (2007). *Demonstration of clean particle seeding for particle image velocimetry in a closed circuit supersonic wind tunnel*. MS thesis, AFIT/GAE/ENY/07-M19. Graduate School of Engineering and Management, Air Force Institute of Technology, Wright-Patterson AFB OH.
- Melling, A. (1997). Tracer particles and seeding for particle image velocimetry. *Measurement Science & Technology*, 8(12), 1406-1416.

- Mokry, M., and Yeung, A.F.K. (1999). On the Evolution of Trailing Vortex Sheets. *ESAIM:Proceedings*, Vol. 7, 1999, 292-303.
- Peltier, D. (2007). *Performing particle image velocimetry in a supersonic wind tunnel using carbon dioxide as the seed material*. MS thesis, AFIT/GAE/ENY/07-J17. Graduate School of Engineering and Management, Air Force Institute of Technology, Wright-Patterson AFB OH.
- Raffel, M. (1998). *Particle Image velocimetry, a practical guide*. Verlag, Berlin, Heidelberg: Springer.
- Rawle, A. *Basic principles of particle size analysis*. Malvern Instruments Limited, Worcestershire, UK.
- Scaran, F. and van Oudheusden, B. (2003). Planar velocity measurements of a two-dimensional compressible wake. *Experiments in Fluids*, 34(3), 430-441.
- Schlichting, H. (1979). *Boundary layer theory*, New York: McGraw-Hill.
- Spraytec Users Manual (2006). Malvern Instruments Limited, Worcestershire, UK.
- Swain, E., Carter, S. and Hoenig, S. *Carbon dioxide snow agglomeration and acceleration*. Excerpt from patent summary. <http://www.freepatentsonline.com/5125979.html>. November 2007.
- Tropea, C., Yarin, A. and Foss, J. (2007). *Springer handbook of experimental fluid mechanics*. Verlag, Berlin, Heidelberg: Springer.

## **Vita**

2<sup>nd</sup> Lieutenant Bartt G. Greene graduated from the United States Naval Academy in Annapolis, Maryland on May 25<sup>th</sup>, 1994 with a Bachelor of Science degree in Mathematics. He was commissioned a Second Lieutenant in the United States Marine Corps on the same day. 2<sup>nd</sup> Lieutenant Greene completed the Basic School in November of 1994 and reported for flight training in December of 1994. 1<sup>st</sup> Lieutenant Greene earned his wings of gold in May of 1997.

Upon completion of AV-8B Harrier fleet replacement pilot training in Cherry Point, North Carolina, Captain Greene reported to Marine Corps Air Station Yuma, Arizona where he served with VMA-311 from October 1998 to February 2002. During this period he participated in a six-month deployment to Iwakuni, Japan in which the Squadron(-) supported the 31<sup>st</sup> Marine Expeditionary Unit (Special Operations Capable). During this period, Captain Greene supported operations in the Pacific in support of the Global War on Terrorism.

In February 2002, Captain Greene reported to 3<sup>rd</sup> Battalion, 4<sup>th</sup> Marines in 29 Palms, California where he served as the Battalion's Air Officer. In January of 2003, he deployed with the battalion in support of Operation Iraqi Freedom I (OIF I) and participated in battles throughout Iraq to include Basra, Al Kut and Baghdad. Captain Greene returned to 29 Palms in May of 2003 and upon his return from OIF, he reported to Marine Air Group 13 in July of 2003. After completing a refresher course of training at VMAT-203 in September of 2003, he reported to VMA-311 where he served as the Assistant Operations Officer, Pilot Training Officer, Director of Safety and



Standardization and as the Aircraft Maintenance Officer. In October 2004, Major Greene deployed to Marine Corps Air Station Al Asad, Iraq where he served in support of Operation Iraqi Freedom II, including Operation Urgent Fury in Fallujah. Major Greene returned to Yuma with VMA-311 in May of 2005 where he served out his tour as the Aircraft Maintenance Officer. In May of 2006 Major Greene reported to the Air Force Institute of Technology to obtain his Master's of Science degree in Aeronautical Engineering.

Major Greene has over 1200 flight hours in the AV-8B Harrier. He holds the advance flight qualifications of Night Systems Instructor (NSI), Air Combat Maneuvering Flight Leader (ACMFL), Low Altitude Tactics Instructor (LATI) and Division Leader. He attended the 2-04 Weapons and Tactics Course at Marine Aviation Weapons and Tactics Squadron and earned his Weapons and Tactics Instructor (WTI) qualification in April of 2004. He is also a day, basic Landing and Signals Officer. His personal decorations include the Air Strike Medal with numeral 6, Navy and Marine Corps Commendation Medal with combat distinguishing device, the Navy and Marine Corps Achievement Medal and the Combat Action Ribbon.

REPORT DOCUMENTATION PAGE				Form Approved OMB No. 074-0188	
<p>The public reporting burden for this collection of information is estimated to average 1 hour per response, including the time for reviewing instructions, searching existing data sources, gathering and maintaining the data needed, and completing and reviewing the collection of information. Send comments regarding this burden estimate or any other aspect of the collection of information, including suggestions for reducing this burden to Department of Defense, Washington Headquarters Services, Directorate for Information Operations and Reports (0704-0188), 1215 Jefferson Davis Highway, Suite 1204, Arlington, VA 22202-4302. Respondents should be aware that notwithstanding any other provision of law, no person shall be subject to a penalty for failing to comply with a collection of information if it does not display a currently valid OMB control number.</p> <p><b>PLEASE DO NOT RETURN YOUR FORM TO THE ABOVE ADDRESS.</b></p>					
1. REPORT DATE (DD-MM-YYYY) 14 Mar 08		2. REPORT TYPE Master's Thesis		3. DATES COVERED (From – To) March 2007– Jun 2008	
4. TITLE AND SUBTITLE  CHARACTERIZATION AND CONTROL OF CARBON DIOXIDE SEED PARTICLES IN PARTICLE IMAGE VELOCIMETRY				5a. CONTRACT NUMBER 07 - 301	
				5b. GRANT NUMBER	
				5c. PROGRAM ELEMENT NUMBER	
6. AUTHOR(S)  Greene, Bartt G, Major, USMC				5d. PROJECT NUMBER	
				5e. TASK NUMBER	
				5f. WORK UNIT NUMBER	
7. PERFORMING ORGANIZATION NAMES(S) AND ADDRESS(S) Air Force Institute of Technology Graduate School of Engineering and Management (AFIT/EN) 2950 Hobson Way WPAFB OH 45433-7765				8. PERFORMING ORGANIZATION REPORT NUMBER  AFIT/GAE/ENY/08-M12	
9. SPONSORING/MONITORING AGENCY NAME(S) AND ADDRESS(ES) James Grove (937.785.8484, James.Grove@WPAFB.AF.MIL) CAPT Chris McGaha, USAF (Christopher.McGaha@AFIT.EDU) AFRL/RB WPAFB OH 45433				10. SPONSOR/MONITOR'S ACRONYM(S)	
				11. SPONSOR/MONITOR'S REPORT NUMBER(S)	
12. DISTRIBUTION/AVAILABILITY STATEMENT APPROVED FOR PUBLIC RELEASE; DISTRIBUTION UNLIMITED.					
13. SUPPLEMENTARY NOTES					
14. ABSTRACT <p>Carbon Dioxide (CO<sub>2</sub>) particles exiting from a variety of feed tube and shroud configurations, and in combination with varying volumetric flow rates of purge air were measured using a laser diffraction device. CO<sub>2</sub> particles were then injected into the stilling chamber of two open-circuit blow down supersonic wind tunnels to obtain PIV measurements. A ten degree ramp placed in the test section of one wind tunnel produced a shock wave which allowed for the characterization of the time response of the CO<sub>2</sub> particles as they crossed the shock wave. This time response was compared with theoretical time responses of varying diameter CO<sub>2</sub> particles in order to characterize the spherical diameter of the actual CO<sub>2</sub> particles. Purge air was used to demonstrate the ability to alter the size of particles by altering the time response of the particles across the shock wave. A scale up was performed to demonstrate the applicability of the clean seeding technique to different size wind tunnels. Initial particle measurements demonstrate the ability to control the size of CO<sub>2</sub> particles which is backed up by actual PIV measurements confirming size characterization.</p>					
15. SUBJECT TERMS Particle Image Velocimetry, Particle Size, Carbon Dioxide, Clean Seeding, Supersonic Wind Tunnel, Particle Relaxation, Boundary Layer					
16. SECURITY CLASSIFICATION OF:			17. LIMITATION OF  ABSTRACT  UU	18. NUMBER OF PAGES  102	19a. NAME OF RESPONSIBLE PERSON Dr. Mark F. Reeder (AFIT/ENY)
REPORT U	ABSTRACT U	c. THIS PAGE U			19b. TELEPHONE NUMBER (Include area code) (937) 255-3636, ext 4530; e-mail: Mark.Reeder@afit.edu

**Standard Form 298 (Rev: 8-98)**

Prescribed by ANSI Std. Z39-18